chapter 3

NANOCRYSTALLINE SOFT MAGNETIC ALLOYS

GISELHER HERZER

Vacuumschmelze GmbH
D-63450 Hanau
Germany

CONTENTS

Abstract

Nanocrystalline structures offer a new opportunity for tailoring soft magnetic materials. This chapter surveys the state of the art and the key factors from which the extraordinary properties of this new class of soft ferromagnets derive. The materials to be discussed are produced by crystallization from the amorphous state and are based on iron. The alloy system in particular highlighted will be the originally proposed Fe–Cu–Nb–Si–B alloys which owing to their outstanding properties have meanwhile successfully entered into application. The general features shown up, however, also apply to other nanocrystalline magnetic materials.

1. Introduction

In 1988, Yoshizawa, Oguma and Yamauchi introduced a new class of *iron* based alloys exhibiting superior soft magnetic behavior. The properties were a unique combination of the low losses, high permeability and near zero magnetostriction achieved by permalloys and Co-based amorphous alloys, but with a saturation magnetization up to 1.3 Tesla – much higher than either of these materials can conventionally offer. The particular about the new material was its ultrafine microstructure of b.c.c. Fe–Si with grain sizes of 10–15 nm from which their soft properties lastly derive and after which they were named *nanocrystalline*.

The material was produced by crystallization of an amorphous Fe–Si–B alloy with small additions of Cu and Nb, a hitherto somewhat unusual combination which proved to be key for the particular ultrafine grain structure and the associated soft magnetic properties. The result was surprising. So far, the crystallization of amorphous metals optimized for soft magnetic application was rather known to deteriorate the soft magnetic properties significantly and to yield a relatively coarse microstructure with grain sizes of about 0.1–1 μm. Only slightly partially crystallized amorphous Fe-base alloys were seen to offer eventual benefits over the amorphous state for certain high frequency applications (cf. Hasegawa et al. 1982, Herzer and Hilzinger 1986).

It is well known that the microstructure, noticeably the grain size, essentially determines the hysteresis loop of a ferromagnetic material. Figure 1.1 summarizes our present understanding of the coercivity, H_c, in the whole range of structural correlation lengths starting from atomic distances in amorphous alloys over grain sizes, D, in the nanometer regime up to macroscopic grain sizes – the permeability shows an analogous behavior being essentially inversely proportional to H_c. The $1/D$-dependence of coercivity for large grain sizes (cf. Pfeifer and Radeloff 1980) reflects the conventional rule that good
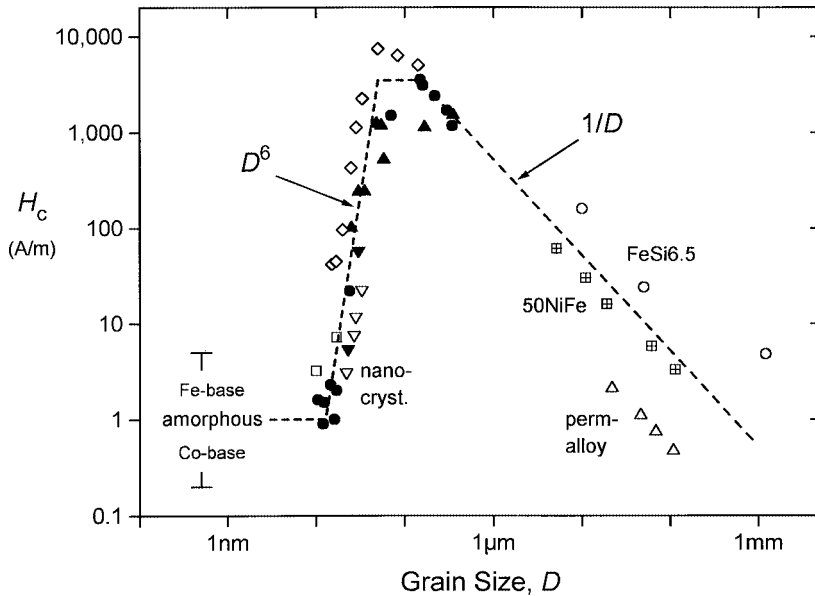
Fig. 1.1. Coercivity, H_c, vs. grain size, D, for various soft magnetic metallic alloys: Fe–Nb–Si–B (solid up triangles, Herzer 1990), Fe–Cu–Nb–Si–B (solid circles, Herzer 1990–1995 and Herzer and Warlimont 1992), Fe–Cu–V–Si–B (solid and open down triangles, this work and Sawa and Takahashi 1990, respectively), Fe–Zr–B (open squares, Suzuki et al. 1991), Fe–Co–Zr (open diamonds, Guo et al. 1991), NiFe alloys (+ center squares and open up triangles, Pfeifer and Radeloff 1980) and Fe–Si(6.5 wt%) (open circles, Arai et al. 1984).

soft magnetic properties require very large grains ($D > 100$ μm). Thus, the reduction of particle size to the regime of the domain wall width increases the coercivity H_c towards a maximum controlled by the anisotropies present. Accordingly, fine particle systems have been mostly discussed as hard magnetic materials (cf. Luborsky 1961). Lowest coercivities, however, are again found for smallest structural correlation lengths like in amorphous alloys ("grain size" of the order of atomic distances) and in nanocrystalline alloys for grain sizes $D < 20$ nm. Obviously, the new nanocrystalline material fills in the gap between amorphous metals and conventional poly-crystalline alloys. The extraordinary D^6-dependence of coercivity at small grain size moreover demonstrates how closely soft and hard magnetic behavior actually can be neighbored. Indeed, the soft magnetic alloys are only one manifestation of the novel and extraordinary magnetic properties which can be realized by establishing structural features on the nanometer scale. Thus, nanocrystalline microstructures are also of highly current interest in order to enhance the properties of rare earth hard magnets (cf. Kneller and Hawig 1991 and Manaf et al. 1993).

   The combination of small grain size and soft magnetic properties is surprising and fascinating from the classical point of view in magnetic engineering. Yet, this possibility was principally known from amorphous materials and the theoretical interpretation of their soft magnetic properties by Alben, Becker and Chi (1978). Accordingly, magnetic

TABLE 1.1

Typical values of grain size D, saturation magnetization J_s, saturation magnetostriction λ_s, coercivity H_c, initial permeability μ_i, electrical resistivity ρ, core losses P_{Fe} at 0.2 T, 100 kHz and ribbon thickness t for nanocrystalline, amorphous and crystalline soft magnetic ribbons.

Alloy	D (nm)	J_s (T)	λ_s (10^{-6})	H_c (A/m)	μ_i (1 kHz)	ρ ($\mu\Omega$ cm)	P_{Fe} (W/kg)	t (μm)	Ref.
$Fe_{73.5}Cu_1Nb_3Si_{13.5}B_9$	13	1.24	2.1	0.5	100 000	118	38	18	(a)
$Fe_{73.5}Cu_1Nb_3Si_{15.5}B_7$	14	1.23	~ 0	0.4	110 000	115	35	21	(b)
$Fe_{84}Nb_7B_9$	9	1.49	0.1	8	22 000	58	76	22	(c)
$Fe_{86}Cu_1Zr_7B_6$	10	1.52	~ 0	3.2	48 000	56	116	20	(c)
$Fe_{91}Zr_7B_3$	17	1.63	-1.1	5.6	22 000	44	80	18	(c)
$Co_{68}Fe_4(MoSiB)_{28}$	amorphous	0.55	~ 0	0.3	150 000	135	35	23	(b)
$Co_{72}(FeMn)_5(MoSiB)_{23}$	amorphous	0.8	~ 0	0.5	3 000	130	40	23	(b)
$Fe_{76}(SiB)_{24}$	amorphous	1.45	32	3	8 000	135	50	23	(b)
80% Ni–Fe (permalloys)	$\sim 100 000$	0.75	< 1	0.5	100 000 (d)	55	> 90 (e)	50	(b)
50%–60% Ni–Fe	$\sim 100 000$	1.55	25	5	40 000 (d)	45	> 200 (e)	70	(b)

(a) Yoshizawa, Oguma and Yamauchi 1988.
(b) Typical commercial grades for low remanence hysteresis loops, Vacuumschmelze GmbH 1990, 1993.
(c) Suzuki et al. 1991, 1993.
(d) 50 Hz-values.
(e) Lower bound due to eddy currents.

softening should also occur as soon as the structural correlation length or grain size becomes smaller than the ferromagnetic exchange length which is in the order of the domain wall width. In this case the local anisotropies are randomly averaged out by exchange interaction so that there is no anisotropy net effect on the magnetization process.

The decrease of coercivity in the new nanocrystalline materials has to be well distinguished from superparamagnetic phenomena i.e., the well-known decrease of coercivity in small, isolated or weakly coupled particles due to thermal excitation (Kneller 1969, Luborsky 1961). Although coercivity vanishes, the superparamagnetic regime is not very interesting for soft magnetic application since an appreciable change of magnetization requires large magnetic fields, i.e., the permeability is fairly low. In the present case we deal with small ferromagnetic crystallites well coupled by exchange interaction and with low coercivity and simultaneously high permeability.

The pioneering discovery of Yoshizawa and co-workers (1988) stimulated an intensive and still ongoing research for alternative alloy compositions. Thus, low-magnetostrictive nanocrystalline Fe–(Cu)–Zr–B alloys (Suzuki et al. 1991) or Fe–Hf–C thin films (Hasegawa and Saito 1991, Hasegawa et al. 1992) have been established which exhibit a still higher saturation magnetization up to 1.7 Tesla due to the higher Fe content in the alloy. Still, the outstanding soft magnetic properties of the original alloy system could not be reached up to now. Interestingly, as a kind of precursor, the first example for soft magnetic behavior in the nanocrystalline state was given by O'Handley et al. (1985) for a devitrified glassy *cobalt* base alloy. However, the soft magnetic properties were inferior to the amorphous state and, thus, not very attractive, which to the present seems to be typical for cobalt based nanocrystalline materials. Indeed, the most promising properties so far have been found in *iron* based alloys. Table 1.1 summarizes some examples and their magnetic properties in comparison with conventional soft magnetic alloys.

2. Preparation and basic characteristics

Principally, nanocrystalline alloys can be synthesized by a variety of techniques such as rapid solidification from the liquid state, mechanical alloying, plasma processing and vapor deposition (cf. Suryanarayana 1995). Yet the requirements on the microstructure necessary for the soft magnetic properties rule out quite a number of the available processes. Thus, Kuhrt and Schultz (1993) have shown, that mechanical alloying seems to be unsuitable for the production of soft magnetic nanocrystalline Fe–Co and Fe–Ni because of the considerable introduction of internal strain into the material which is inevitably related to the process and cannot be removed without the simultaneous occurrence of undesirable grain growth. Compacted nanometer sized powders prepared by inert gas condensation techniques (Birringer and Gleiter, 1988), although frequently discussed, are also unsuitable for obtaining good soft magnetic properties due to the unfavorable intergranular linkage which considerably reduces the necessary ferromagnetic coupling between the grains.

Actually, controlled crystallization from the amorphous state seems to be the only method presently available to synthesize nanocrystalline alloys with attractive soft magnetic properties. The amorphous pre-cursor material is prepared either as a thin film by sputtering techniques or, on which we will focus here, as a ribbon by rapid solidification

from the melt – a meanwhile well established technique for large scale production of amorphous metals.

A typical nanocrystalline structure with good soft magnetic properties occurs if the amorphous state is crystallized by the primary crystallization of b.c.c. Fe, before inter-metallic phases like Fe–B compounds may be formed. Both an extremely high nucle-ation rate and slow growth of the crystalline precipitates are needed in order to obtain a nanoscaled microstructure. Such a crystallization characteristics seems to be rather the exception than the rule. Thus, crystallization of conventional metallic glasses optimized for soft magnetic applications usually yields a relatively coarse grained microstructure of several crystalline phases and, correspondingly, deteriorates the soft magnetic properties. Although it appears to be possible to refine the microstructure of such conventional com-positions by special annealing techniques like pulse-heating (cf. Kulik et al. 1992), such methods are less suitable in view of reproducibility and application. What is needed, is a controlled crystallization behavior upon isothermal annealing which is relatively in-sensitive to the precise annealing conditions. This can be lastly only achieved by an appropriate alloy design, in particular, by alloying special elements which promote the nucleation of b.c.c. Fe, retard the grain growth and simultaneously inhibit the formation of intermetallic phases. The requirement of a good glass forming ability puts further constraints on the accessible alloy compositions.

2.1. Fe–Cu–Nb–Si–B alloys

The optimum alloy composition originally proposed and subsequently not much changed is $Fe_{73.5}Cu_1Nb_3Si_{13.5}B_9$ (at%) and can be considered as a typical Fe–Si–B metallic glass composition with small additions of Cu and Nb. The alloy system has a good glass forming ability and is easily accessible by rapid solidification as an originally amorphous ribbon, typically 20 μm thick.

2.1.1. Formation of the nanocrystalline state

Figure 2.1 summarizes the evolution of the microstructure and the soft magnetic proper-ties with the annealing temperature; examples of characteristic microstructures are shown in fig. 2.2.

The nanocrystalline state is achieved by annealing at temperatures typically between about 500°C and 600°C which leads to primary crystallization of b.c.c. Fe. The re-sulting microstructure is characterized by randomly oriented, ultrafine grains of b.c.c. Fe–Si(20 at%) with typical grain sizes of 10–15 nm embedded in a residual amorphous matrix which occupies about 20–30% of the volume and separates the crystallites at a distance of about 1–2 nm. These features are the basis for the excellent soft mag-netic properties indicated by the high values of the initial permeability of about 10^5 and correspondingly low coercivities of less than 1 A/m.

A characteristic feature is that the nanocrystalline microstructure and the accompanying soft magnetic properties are rather insensitive to the precise annealing conditions within a wide range of annealing temperatures, T_a, of about $\Delta T_a \approx 50–100°C$. They develop in a relatively short period of time (about 10–15 min) and do not much alter even after prolonged heat treatment of several hours (cf. Yoshizawa and Yamauchi 1991a). A typical
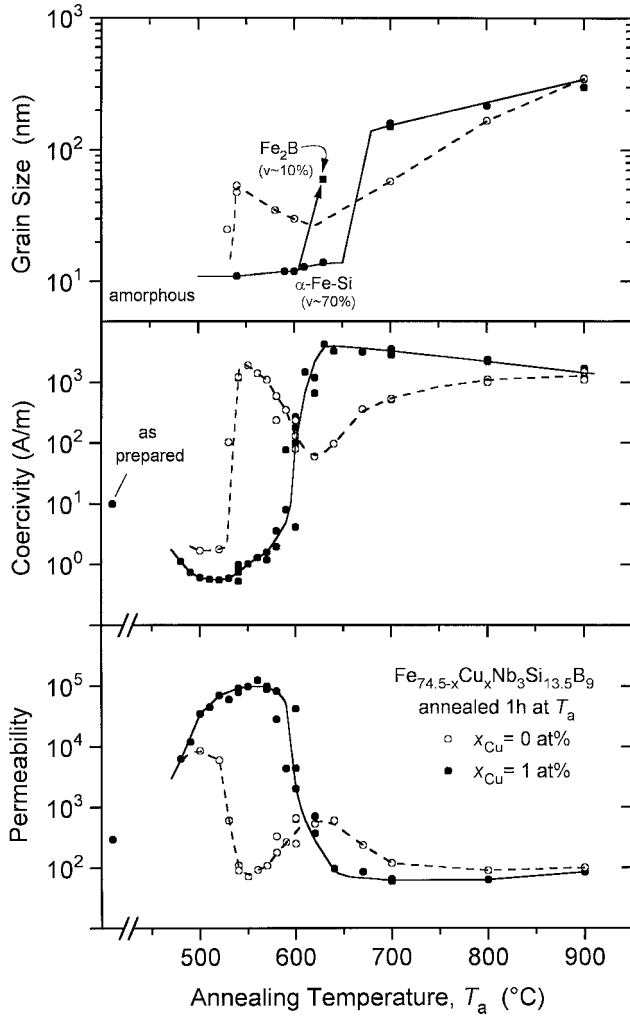
Fig. 2.1. Average grain size, coercivity and initial permeability of $Fe_{74.5-x}Cu_xNb_3Si_{13.5}B_9$ ($x = 0$ and 1 at%) as a function of the annealing temperature.

heat treatment like 1h at 540°C in most cases yields a nanocrystalline microstructure close to the quasi-equilibrium state and characteristic for the individual alloy composition.

Only annealing at more elevated temperatures above about 600°C leads to the precipitation of small fractions of boride compounds like Fe_2B or Fe_3B with typical dimensions of 50 nm to 100 nm, while the ultrafine grain structure of b.c.c. Fe–Si still persists. Further increase of the annealing temperature above about 700°C, finally yields grain coarsening. Both the formation of Fe borides and grain coarsening deteriorates the soft magnetic properties significantly.
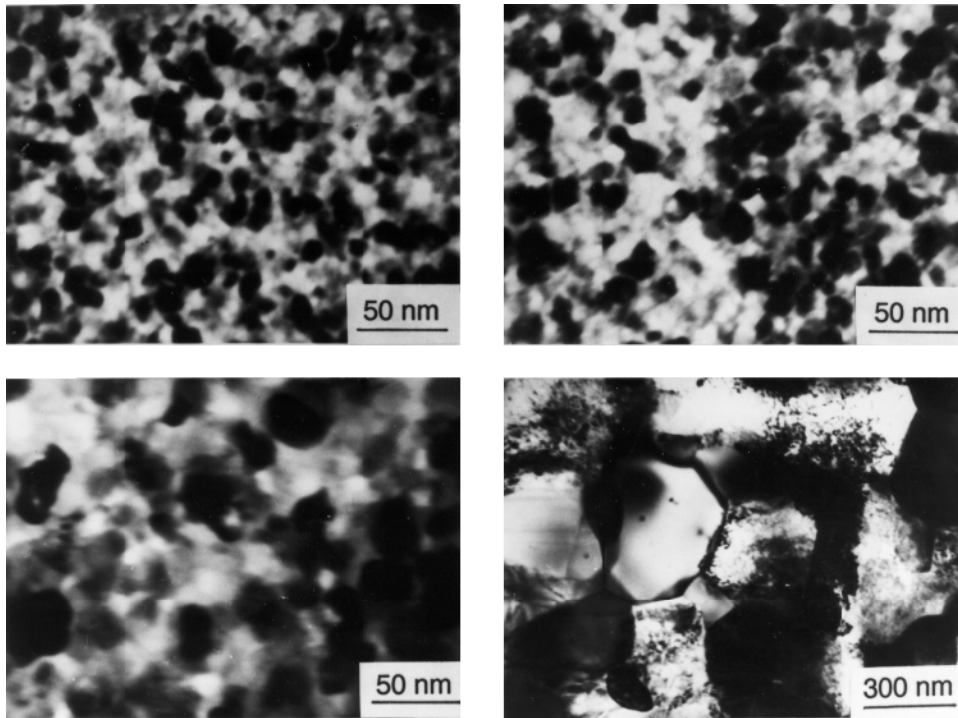
Fig. 2.2. Transmission electron bright field micrographs of Fe–Cu–Nb–Si–B alloys showing various stages of crystallization with good (upper row) and deteriorated (lower row) soft magnetic properties. Upper row: $Fe_{73.5}Cu_1Nb_3Si_{13.5}B_9$ (left) and $Fe_{73.5}Cu_1Nb_3Si_{16.5}B_6$ (right) annealed at $540°C$. Lower row: $Fe_{74.5}Nb_3Si_{13.5}B_9$ annealed at $530°C$ (left) and $Fe_{73.5}Cu_1Nb_3Si_{13.5}B_9$ annealed at $900°C$ (right). The annealing time was 1 h in each case.

The formation of the particular nanocrystalline structure is essentially related to the combined addition of Cu and Nb (or other group IV to VI elements) and their low solubility in b.c.c. Fe–Si: copper enhances the nucleation of the b.c.c. grains while niobium impedes coarsening and, at the same time, inhibits the formation of boride compounds. The microstructure evolution is schematically illustrated in fig. 2.3 and can be summarized as follows:

The phase separation tendency between Cu and Fe leads to the formation of Cu-rich clusters, about 5 nm in size and probably still amorphous, in the initial stage of annealing before the onset of the primary crystallization of the b.c.c. Fe–Si phase (Hono et al. 1992, Hono and Sakurai 1995). The presence of Nb, hereby seems to promote the formation of these Cu-rich clusters on a much finer scale than in an Nb-free alloy composition (Ayers et al. 1994). This cluster formation causes a concentration fluctuation of Fe, since Cu substitutes for Fe. Thus, the regions in between the Cu-rich clusters provide a significantly increased density of nucleation sites for the crystallization of b.c.c. Fe. The consequence is an extremely fine nucleation of b.c.c. Fe–Si crystallites at a high
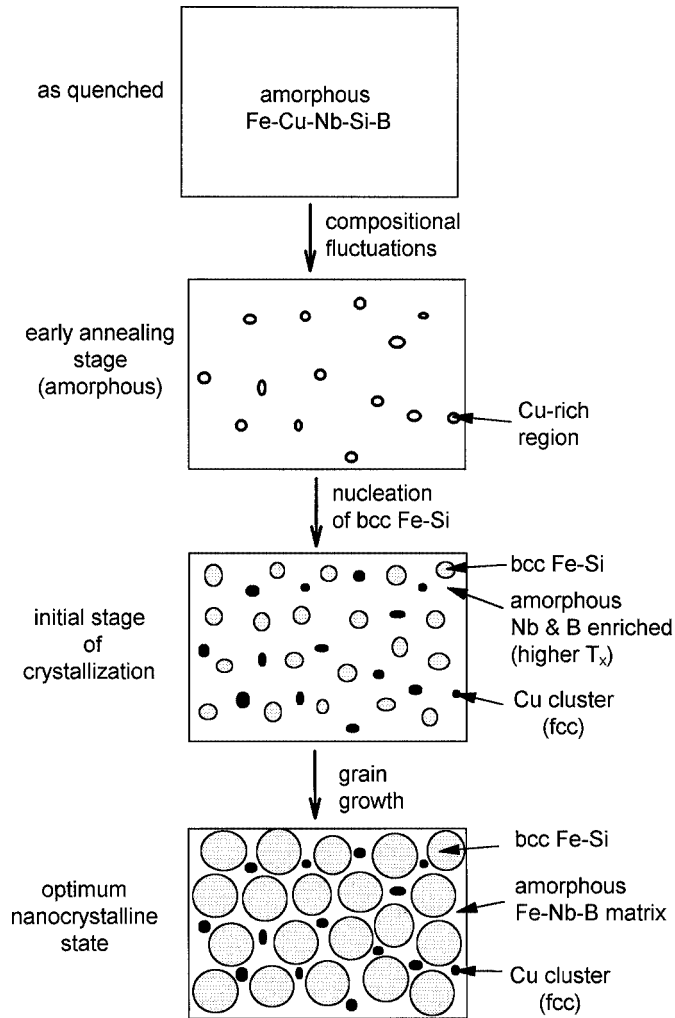
Fig. 2.3. Schematic illustration of the formation of the nanocrystalline structure in Fe–Cu–Nb–Si–B alloys based on atom probe analysis results and transmission electron microscopy observations by Hono et al. 1992, Hono and Sakurai 1995.

rate which subsequently grow in a diffusion controlled process (cf. Köster et al. 1991) as the annealing proceeds further. As the b.c.c. Fe–Si phase forms, Nb and B are excluded from the crystallites because of their low solubility in b.c.c. Fe–Si and are enriched in the residual amorphous matrix. At the same time effectively all Si tends to be partitioned into the b.c.c. Fe–Si phase (Herzer 1991, Hono et al. 1992). The enrichment with B and, in particular, with Nb increasingly stabilizes the residual amorphous matrix and, thus, hinders coarsening of the b.c.c. grains. The presence of Nb at the same time inhibits the
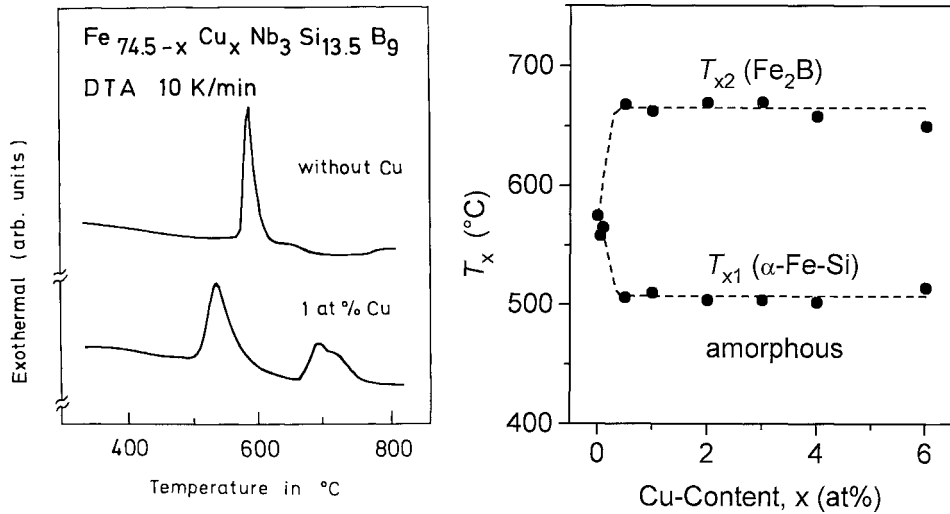
Fig. 2.4. Effect of copper on the crystallization behavior in $Fe_{74.5-x}Cu_xNb_3Si_{13.5}B_9$: (left) typical differential thermo-analysis plots and (right) onset temperatures for crystallization, T_x, vs. the copper content.

formation of Fe boride compounds. The transformation finally ceases in a meta-stable two-phase microstructure of b.c.c. Fe–Si embedded in an amorphous Fe–Nb–B matrix.

The significance of the Cu addition becomes apparent from fig. 2.1 which, for comparison, includes the data for an $Fe_{74.5}Nb_3Si_{13.5}B_9$ alloy, i.e., a similar alloy composition, but without Cu. The crystallization behavior of this Cu-free alloy is quite different and leads to a severe degradation of the soft magnetic properties compared to the original amorphous state. It, thus, resembles much to that what is usually observed in conventional amorphous alloys. The average grain size upon the onset of crystallization is relatively large, up to about 60 nm with a broad scatter, and shows a distinct variation with the annealing temperature. This indicates a significantly lower nucleation rate than in the Cu-doped alloy whose finer grain size is almost constant in a wide range of annealing temperatures. Furthermore, annealing of the Cu-free alloy leads to the simultaneous or sequential formation of several crystalline phases. Thus, as shown in fig. 2.4, differential thermo-analysis (DTA) of the Cu-free alloy reveals two closely neighbored stages of crystallization, mostly overlapping to a single crystallization peak, which correspond to the precipitation of Fe–B compounds, such as b.c.t. Fe_3B or $Fe_{23}B_6$, in the first and b.c.c. Fe in the second step (cf. Yoshizawa and Yamauchi 1990a, Noh et al. 1990). However, already a small Cu-addition yields two clearly separated crystallization peaks corresponding to the primary crystallization of b.c.c. Fe at T_{x_1} and, subsequently, to the precipitation of Fe_2B compounds at T_{x_2}. The separation between the two peaks is practically insensitive on the further increase of the Cu content beyond a small, critical concentration of about 0.5 at%. The decrease of the onset temperature for the first crystallization stage reflects the local clustering of Cu-atoms which obviously lowers the configurational energy of the subcritical nucleus (Herzer and Warlimont 1992).
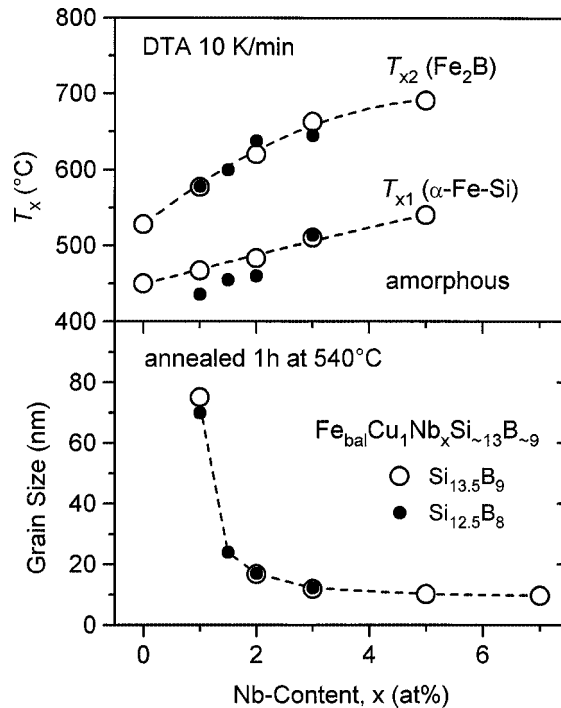
Fig. 2.5. Influence of the Nb content on the onset temperatures, T_x, for crystallization and on the average grain size (open circles after Yoshizawa and Yamauchi 1991b).

The effect of copper in enhancing the nucleation density, in a way, is unique. Gold is the only element which has been verified to have a comparable effect on the crystallization behavior (Kataoka et al. 1989). From this, silver, belonging to the same noble metal group, is expected to behave similarly. However, silver is practically immiscible in iron even in the liquid state, such that alloying of this element into the Fe–Si–B matrix, so far, could not be verified successfully.

Although essential, the Cu-addition alone is not sufficient. Its effect is considerably promoted by the simultaneous presence of Nb. As illustrated in fig. 2.5, Nb enhances the crystallization temperatures and retards the grain growth by limiting diffusion. In particular, the Nb-addition significantly increases the separation between the two crystallization stages which promotes the primary crystallization of b.c.c. Fe and stabilizes the residual amorphous matrix against the precipitation of Fe–B compounds. All together leads to an increased number of simultaneously growing and competing crystals resulting in the nanoscaled microstructure upon alloying at least about 2–3 at% of Nb.

Niobium can be substituted by other group V or VI refractory elements, like Cr, V, Mo, W or Ta which act similarly on the crystallization process and on the magnetic properties (Yoshizawa and Yamauchi 1991b). Like for Nb, the atomic volumes of these refractory elements are larger than that of Fe which reduces the diffusion coefficients and, thus,
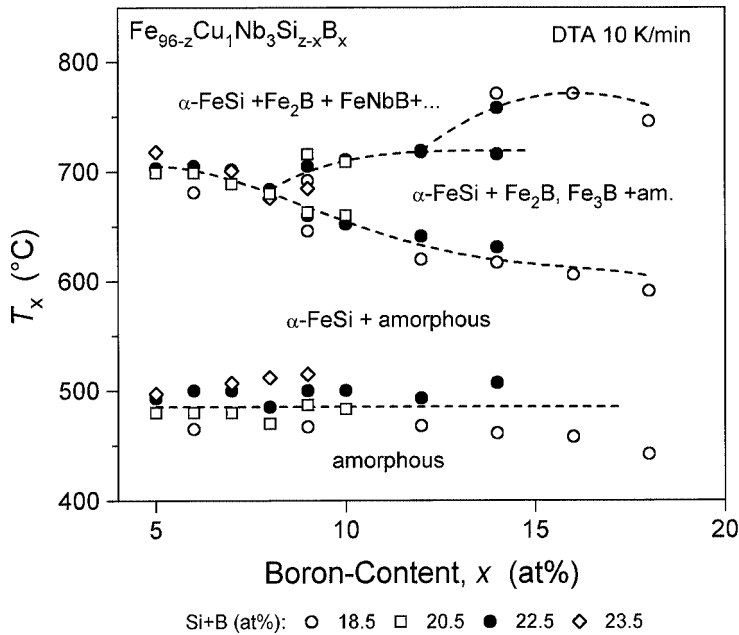
Fig. 2.6. Onset temperatures for crystallization, T_x, vs. the boron content for $Fe_{96-z}Cu_1Nb_3Si_{z-x}B_x$.

stabilizes the amorphous matrix and slows down the kinetics of grain coarsening (Müller and Mattern 1994). Accordingly the efficiency of these elements for grain size refinement increases in the order of their atomic volumes, i.e., $Cr < V < Mo \approx W < Nb \approx Ta$. Thus, finest grain structures and superior magnetic properties in practice require at least a certain amount of the elements Nb or Ta.

It should be stressed again that good soft magnetic properties require not only a small grain size but at the same time the absence of boron compounds. The separation between the primary crystallization of b.c.c. Fe and the precipitation of Fe–B compounds not only is determined by the Cu and Nb additions but, as shown in fig. 2.6, decreases with increasing boron content. This puts a further constraint on the alloy composition namely that the boron content should be kept at a low or moderate level in order to obtain an optimum nanoscaled structure.

In summary, the behavior of the onset of crystallization on temperature and composition shows that a basic condition for the formation of a typical nanocrystalline structure is given by a primary crystallization process before stable or meta-stable intermetallic phases are formed. Obviously, this can be attained by (i) alloying additions which lead to clearly separated stages of crystallization at T_{x_1} and T_{x_2} and (ii) by annealing at $T_{x_1} < T_a < T_{x_2}$ such that only the phase forming at and above T_{x_1} is crystallizing.

2.1.2. Microstructural characteristics

The nanocrystalline microstructure obtained by crystallization from the amorphous state is essentially composed of two phases: (i) the randomly oriented b.c.c. grains and (ii) a still
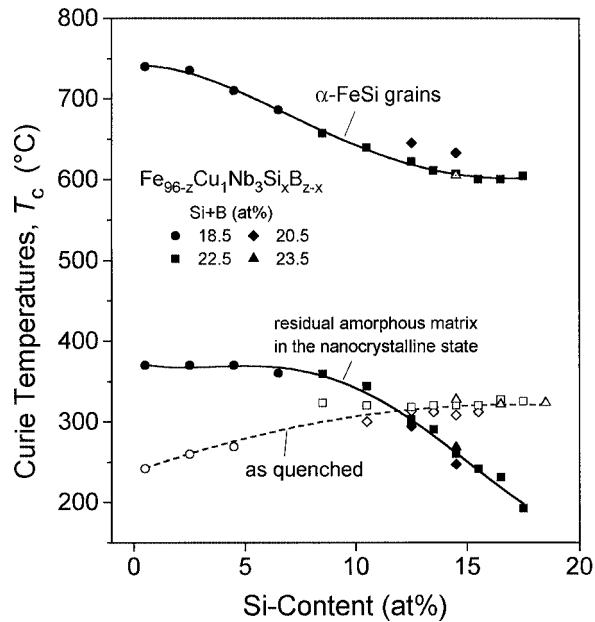
Fig. 2.7. Curie temperatures of the b.c.c.-Fe–Si grains and the residual amorphous matrix in nanocrystalline $Fe_{96-z}Cu_1Nb_3Si_xB_{z-x}$ alloys after annealing 1 h at 540°C (solid symbols). The open symbols show the Curie temperature in the as quenched amorphous state.

amorphous minority matrix. The crystalline fraction and the local atomic concentrations are determined by the original alloy composition.

Since direct chemical analysis, e.g., by electron beam microprobe, is inaccurate on the nanometer scale, lattice parameter and intrinsic property measurements have been evaluated in order to determine the local atomic compositions. In thermodynamical equilibrium, boron is practically insoluble in b.c.c. Fe ($\ll 0.01$ at%); the solubilities of Cu and Nb are low: < 0.2 at% Cu, < 0.1 at% Nb (Kubaschewski 1982). If these values apply to the nanocrystalline phase, too, the b.c.c. grains essentially consist of Fe–Si which is supported by atom probe analysis (Hono et al. 1992). Thus, literature data for lattice parameter, Curie temperature and saturation magnetization of the Fe–Si system (cf. Bozorth 1951 and Yelsukov et al. 1986) may be used to analyze the results obtained for the nanocrystalline state.

Figures 2.7 and 2.8 show the Curie temperatures and the room temperature magnetization of Fe–Cu–Nb–Si–B alloys in the amorphous and in the nanocrystalline state (cf. Herzer 1989, 1991). The precipitation of the b.c.c. Fe–Si phase is clearly manifested in a significant increase of the Curie temperature from 250–320°C in the original amorphous state to about 600–740°C after nanocrystallization. The residual amorphous matrix is ferromagnetic. Its Curie temperature and saturation magnetization, however, are clearly distinct from that of the original amorphous matrix which indicates a significant change in composition.
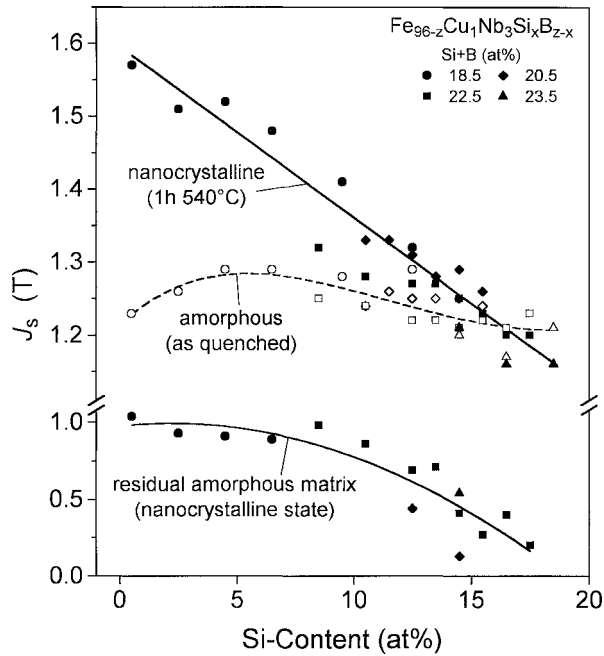
Fig. 2.8. Room temperature saturation magnetization, J_s, of $Fe_{96-z}Cu_1Nb_3Si_xB_{z-x}$ in the as quenched amorphous (open symbols) and nanocrystalline state after annealing 1 h at 540°C (solid symbols, upper part). The lower part of the figure shows the local magnetization of the residual amorphous matrix in the nanocrystalline state (note the change in the axis scale).

Figures 2.9 and 2.10 show the crystalline fraction and the Si content of the crystallites as evaluated from thermomagnetic investigations by comparison with literature data for α-Fe–Si (Herzer 1989, 1991). X-ray investigations of Ueda et al. (1994) give comparable results.

The crystalline fraction, ν_{cr} is mainly determined by the boron content and independent of the Si content. Both the crystalline fraction and the average grain size decreases with increasing boron content. This indicates that the boron plays a similar role as Nb in retarding the grain growth. The average spacing between the crystallites, δ, i.e., the thickness of the intergranular amorphous layer can be estimated by (Herzer 1989)

$$\delta = D(1/\nu_{cr}^{1/3} - 1) \underset{\nu_{cr}\to 1}{\approx} (1 - \nu_{cr})/3 \qquad (2.1)$$

and typically ranges between about 1–2 nm, i.e., about 5–10 atomic layers.

The local Si content in the b.c.c. grains is considerably larger than the average Si content of the alloy. For the high Si content alloys the composition of the b.c.c. grains is close to stoichiometric Fe_3Si which results in a DO_3 superlattice structure (Müller
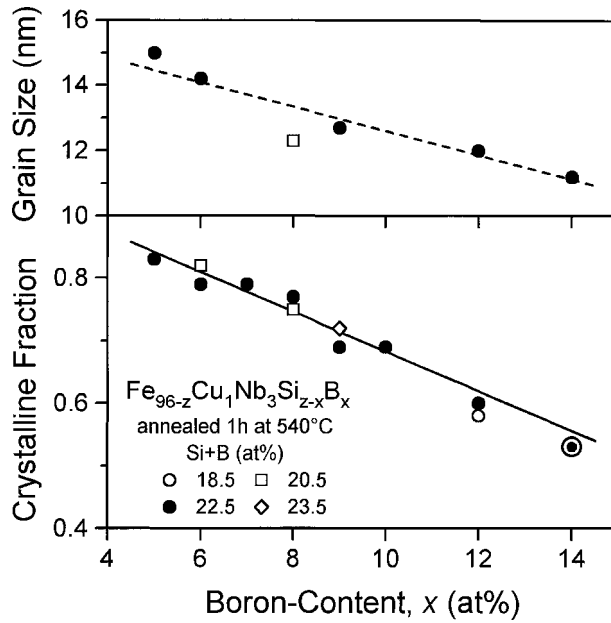
Fig. 2.9. Average grain size and crystalline fraction in nanocrystalline $Fe_{96-z}Cu_1Nb_3Si_{z-x}B_x$ alloys vs. the boron content. The solid line is the crystalline fraction calculated from the balance of atomic concentrations according to the reaction given by eq. (2.3) with $n = 2.2$.
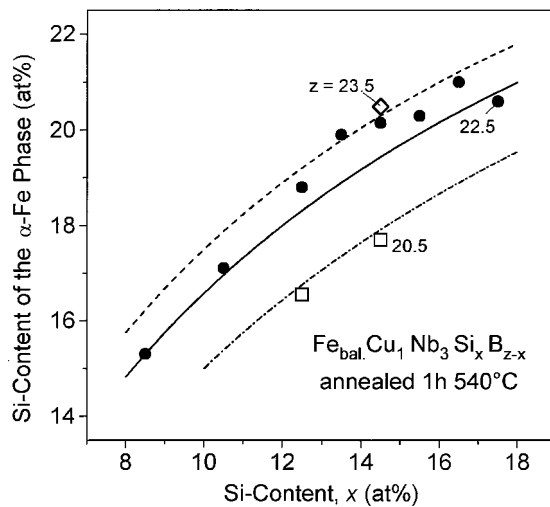

Fig. 2.10. Local Si content in the b.c.c. grains of nanocrystalline $Fe_{96-z}Cu_1Nb_3Si_xB_{z-x}$ alloys vs. the Si content. The lines correspond the theoretical result from the balance of atomic concentrations according to the reaction given by eq. (2.3) with $n = 2.2$.
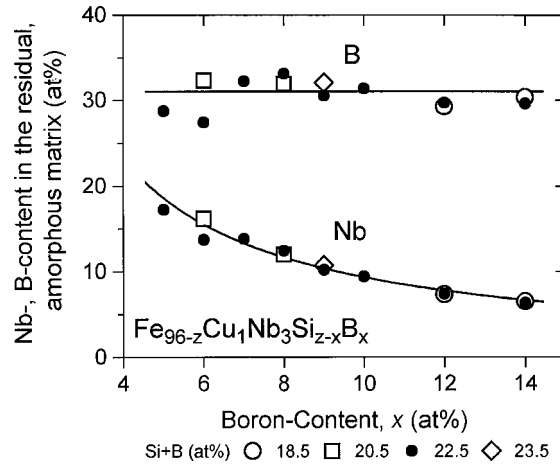
Fig. 2.11. Local boron and niobium content in the residual amorphous matrix vs. the boron content as estimated by balance of atomic concentrations. The symbols are based on the experimental data of the crystalline fraction, the solid lines result from the reaction proposed in eq. (2.3) assuming $n = 2.2$.

et al. 1991, Hampel et al. 1992). The Si content in the b.c.c. grains, y_{Si}(b.c.c.), can be approximately related to the average Si content, x_{Si}, by

$$y_{Si}(\text{b.c.c.}) \approx x_{Si}/\nu_{cr} \qquad (2.2)$$

which indicates that effectively all Si has partitioned into the crystallites (Herzer 1991). Accordingly, the amorphous matrix essentially consists of Fe, Nb and B. The formation of the nanocrystalline state, thus, can be lastly characterized by the reaction (Herzer 1993)

$$\text{Fe–Cu–Nb–Si–B} \rightarrow \nu_{cr}\,\alpha\text{-Fe}_{1-y}\text{Si}_y + (1 - \nu_{cr})(\text{Fe}_{1-a}\text{Nb}_a)_n\text{B} + x_{Cu}\,\text{Cu} \qquad (2.3)$$

with $a = n^{-1}x_{Nb}/x_B$ where x_{Nb}, x_{Cu} and x_B denote the alloy's niobium, copper and boron contents, respectively.

Equation 2.3 allows to estimate the composition of the intergranular amorphous phase from the data for the crystalline fraction by balance of atomic concentrations. The result of this evaluation, being shown in fig. 2.11, is a high local boron content of around 31 at% (i.e., $n \approx 2.2$) which is fairly independent of the original alloy composition. Obviously the nucleation and growth of the b.c.c. grains proceeds until the residual amorphous matrix is enriched with boron such that its composition is close to stoichiometric $(\text{Fe}_{1-a}\text{Nb}_a)_2\text{B}$. The presence of niobium hereby stabilizes the amorphous structure and impedes the formation of the corresponding crystalline boride compounds. The local Nb content is independent of the Si content and increases with decreasing average B content. This is a consequence of the simultaneously decreasing amorphous fraction, $\nu_{am} = 1 - \nu_{cr}$, (cf. fig. 2.9) in which the available niobium is enriched. This local enrichment of the Nb lastly signs responsible for the increase of the onset temperature of the second crystallization

stage (fig. 2.6) and the decrease of the Curie temperature (fig. 2.7) and the saturation magnetization (fig. 2.8) of the residual amorphous matrix with decreasing average B content.

2.2. *Further alloy compositions*

A major driving force in the search for further alloy compositions was to increase the saturation magnetization which in the optimized compositions around $Fe_{73.5}Cu_1Nb_3Si_{13.5}B_9$ is limited to about $J_s \approx 1.2$–1.3 T due to the high Si content in the b.c.c. grains. An appreciable increase of J_s, thus, requires a nanocrystalline structure which essentially consists of pure α-iron. The major hindrance towards such high iron content alloys is given by the requirement of a good glass forming ability. Thus, for the sake of a good glass forming ability, the Si content in the Fe–Cu–Nb–Si–B alloys cannot be simply reduced without substituting other glass formers for it.

One way of reducing the Si content is to replace it with boron which is an even better glass forming element than Si. As apparent from fig. 2.8, the saturation magnetization in the $Fe–Cu_1Nb_3Si_xB_{z-x}$ system indeed increases up to about 1.6 T if boron is substituted for silicon. However this benefit is accompanied by a severe degradation of the soft magnetic properties (see section 3). The reason is that the high boron content necessary to replace the silicon at the same time favors the formation of boron compounds (fig. 2.6) which are deleterious for the soft magnetic properties. In order to obtain a homogeneous nanocrystalline b.c.c. structure with good soft magnetic properties it is necessary to keep the boron content at a moderate level below about 10 at%. A low boron content at the same time yields a high crystalline fraction (fig. 2.9) which additionally maximizes the saturation magnetization. However, a corresponding reduction of the boron content at low Si contents, for the sake of glass forming ability, is only possible if other good glass forming elements are added simultaneously. Such elements which extend the glass forming range at low Si and B contents are group IVa to VIa transition metals (Inoue et al. 1981). The glass forming range is the widest for Hf containing alloys and decreases in the order of $Zr > Nb \approx Ta > Mo \approx W > V > Cr$. The most stable amorphous phase is, thus, obtained in alloys containing refractory metals with large atoms and low d-electron concentrations, i.e., particularly Zr, Hf, Nb and Ta. As mentioned before, these elements at the same time are very effective in suppressing the formation of the undesired boride compounds.

Accordingly, high iron content $Fe–(Cu_1)–M_{\sim7}B_{2-9}$ alloys with M = Hf, Zr, Nb, and/or Ta have been found to exhibit both a more or less sufficient glass forming ability and the necessary crystallization characteristics in order to give a nanocrystalline structure with good soft magnetic properties, low magnetostriction and a high saturation induction up to 1.7 T (Suzuki et al. 1991, 1993). Yet these alloys and derivatives are currently still under intensive research. A major problem is still glass forming ability and castability. Thus, the Nb containing alloys which yield reasonable properties, like e.g., $Fe_{84}Nb_7B_9$, are located at the border of the glass forming range (Suzuki et al. 1994) which makes them most difficult to produce in particular on larger scale. The glass forming ability is considerably improved with the addition of Zr or Hf. However, the strong oxygen reactivity of either of the two elements is a severe problem and requires a good protecting casting atmosphere. Moreover, the compositions with the highest saturation magnetization of $J_s = 1.6$–1.7 T,

like $Fe_{91}Zr_7B_2$ are again located at the border of the glass forming range. The preparation of Fe–M–B thin ribbons by rapid solidification, thus, requires substantially more effort than necessary for the more conventional Fe–(Cu, Nb)–Si–B compositions and, therefore, presently is still restricted to the laboratory scale.

Interestingly, in the Fe–M–B alloys the addition of copper is not necessarily required in order to yield a nanocrystalline structure with reasonable magnetic properties. Quenched-in compositional fluctuations in the amorphous state due to a relatively low glass-forming ability and the enhanced concentration of refractory elements insoluble in α-Fe are considered as a possible explanation (Suzuki et al. 1994). Still, the addition of Cu, like previously discussed, again promotes the primary nucleation of the b.c.c. Fe and enhances the soft magnetic properties significantly.

It should be finally mentioned that the spectrum of accessible nanocrystalline systems can still be considerably expanded by thin film sputtering techniques. One example are Hf carbide dispersed nanocrystalline Fe–Hf–C films crystallized from the amorphous state (Hasegawa and Saito 1991, Hasegawa et al. 1993). They combine good thermal stability, good high frequency properties in the MHz range with low magnetostriction and high saturation induction of $J_s = 1.7$ T which can be even increased up to 2.0 T by multilayering these films with Fe. Another example are (Fe, Co, Ni)–(Si, B)–(F, O, N) granular alloy films (cf. Fujimori 1995) which at a saturation induction of about 1 T possess a uniquely high electrical resistivity of 10^3–10^4 $\mu\Omega$ cm which makes them a possible candidate for future high-frequency devices.

3. Microstructure–property relationship

We have already seen (fig. 2.1) that coercivities of less than 1 A/m and initial permeabilities of more than 10^5 can be achieved upon the formation of the nanocrystalline b.c.c. Fe–Si structure. Such superior properties, however, are restricted to particular alloy compositions which, as demonstrated in fig. 3.1, are close to the classical $Fe_{73.5}Cu_1Nb_3Si_{13.5}B_9$ alloy. This variation of the magnetic properties can only be understood in part by the grain size effect shown in fig. 1.1. If the grain size is small enough, further microstructural parameters like the composition and the volume fraction of the individual structural phases take over the control of the soft magnetic properties.

The key factor for understanding the microstructure–property relationship is the understanding of magnetic anisotropies and how they can be controlled. Coercivity, H_c, increases with the anisotropy energy density, K, and the initial permeability, μ_i, shows the inverse behavior. Thus, the basic conditions for good soft magnetic properties generally are low or vanishing magnetic anisotropies of a few J/m^3 only. The angular distribution of the anisotropy axis finally controls the shape of the hysteresis loop.

The relevant anisotropy contributions are in decreasing order of magnitude:
1. Magneto-crystalline anisotropy,
2. Magneto-elastic anisotropies,
3. Creep-induced anisotropies, and
4. Magnetic field induced anisotropies.
In the following sections, we will discuss the impact of the various microstructural features on these anisotropy contributions and the associated soft magnetic properties in
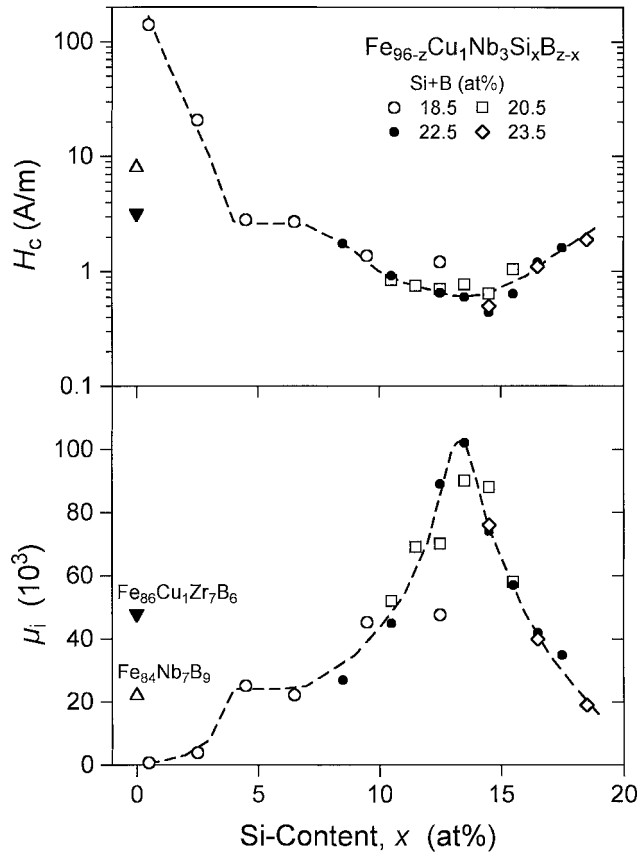
Fig. 3.1. Coercivity, H_c, and initial permeability, μ_i, of nanocrystalline $Fe_{96-z}Cu_1Nb_3Si_xB_{z-x}$ annealed 1 h at 540°C vs. the Si content.

the nanocrystalline state. Thus, the prerequisite for soft magnetic behavior is that the effective magneto-crystalline anisotropy is low. Superior properties additionally require a low magnetostriction which reduces magneto-elastic anisotropies. Once these contributions are sufficiently suppressed, the magnetic properties are determined by uniaxial anisotropies induced during the heat treatment which, if properly controlled, allow to tailor the hysteresis loop according to the demands of application.

3.1. Magneto-crystalline anisotropy

The major requirement for superior soft magnetic behavior generally is a low or vanishing magneto-crystalline anisotropy. The magneto-crystalline anisotropy, K_1, is related to the crystal symmetry; the easy axis of magnetization being determined by the crystal axis. For b.c.c. Fe–Si (20 at%), the constituent phase in nanocrystalline $Fe_{73.5}Cu_1Nb_3Si_{13.5}B_9$, the anisotropy constant is about $K_1 \approx 8$ kJ/m^3 (Gengnagel and Wagner 1961), i.e., by

far too large to explain by itself the low coercivity ($H_c < 1$ A/m) and high permeability ($\mu_i \approx 10^5$).

The key to understand this is that the effective anisotropy contribution of the small, randomly oriented b.c.c. grains is essentially reduced by exchange interaction (Herzer 1989, 1990). The critical scale where the exchange energy starts to balance the anisotropy energy is given by the ferromagnetic exchange length

$$L_0 = \sqrt{A/K_1} \tag{3.1}$$

(A = exchange stiffness constant) which is about $L_0 \approx 35$ nm for the material parameters of b.c.c. Fe–Si(20 at%). L_0 represents the minimum length scale over which the direction of the magnetic moments can vary appreciably and, for example, determines the order of the domain wall width. Thus, if the grain size, D, is reduced below, L_0, the magnetization will not follow the randomly oriented easy axis of the individual grains, but increasingly is forced to align parallel by exchange interaction. As a consequence, the effective anisotropy is an average over several grains and, thus, considerably reduced in magnitude. This makes the essential difference to large grained materials where the magnetization follows the randomly oriented easy axes of the individual grains and, accordingly, the magnetization process is controlled by the full magneto-crystalline anisotropy of the grains.

3.1.1. The random anisotropy model

The degree to which the magneto-crystalline anisotropy is finally averaged out has been successfully addressed in terms of the so-called *random anisotropy model* (Herzer 1989, 1990) which has been originally developed in order to explain the soft magnetic properties of amorphous ferromagnets by Alben et al. (1978). The consequences of the model are so dramatic and of such a technical relevance that the simple, but effective arguments are recast here. A theoretically more sophisticated treatment can be found in the paper of Chudnovsky et al. (1986).

The basic idea is sketched in fig. 3.2 and starts from an assembly of exchange coupled grains of size, D, and volume fraction, ν_{cr}, with magneto-crystalline anisotropies oriented at random. The effective anisotropy constant, $\langle K \rangle$, relevant to the magnetization process results from averaging over the $N = \nu_{cr} (L_{ex}/D)^3$ grains within the ferromagnetic correlation volume $V = L_{ex}^3$ determined by the exchange length L_{ex}. For a finite number, N, of grains within the exchange volume there will be always some easiest direction determined by statistical fluctuations. Thus, the averaged anisotropy energy density is determined by the mean fluctuation amplitude of the anisotropy energy of the N grains, i.e.,

$$\langle K \rangle \approx \frac{\nu_{cr} K_1}{\sqrt{N}} = \sqrt{\nu_{cr}}\, K_1 \left(\frac{D}{L_{ex}} \right)^{3/2}. \tag{3.2}$$

As the local magneto-crystalline anisotropies are averaged out this way, the scale on which exchange interaction dominates expands at the same time. Thus, the exchange
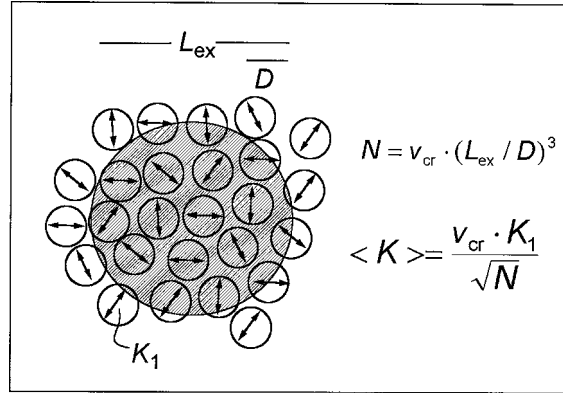
Fig. 3.2. Schematic representation of the random anisotropy model for grains embedded in an ideally soft ferromagnetic matrix. The double arrows indicate the randomly fluctuating anisotropy axis, the hatched area represents the ferromagnetic correlation volume determined by the exchange length $L_{ex} = (A/\langle K \rangle)^{1/2}$.

length, L_{ex}, has to be renormalized by substituting $\langle K \rangle$ for K_1 in eq. (3.1), i.e., L_{ex} is self-consistently related to the averaged anisotropy by

$$L_{ex} = \sqrt{A/\langle K \rangle}. \tag{3.3}$$

The combination of eqs. (3.2) and (3.3) then yields for grain sizes smaller than the exchange length

$$\langle K \rangle \approx \nu_{cr}^2 K_1 (D/L_0)^6 = \nu_{cr}^2 D^6 K_1^4 / A^3. \tag{3.4}$$

It should be noted that this result is essentially based on statistical and scaling arguments and, therefore, is not limited to uniaxial anisotropies (as may be anticipated from fig. 3.2 or from the original work of Alben et al. (1978)) but also applies for cubic or other symmetries.

The most significant feature predicted by the random anisotropy model is the strong variation of $\langle K \rangle$ with the sixth power of the grain size. Thus, for $D \approx L_0/3$, i.e., grain sizes in the order of 10–15 nm, the magneto-crystalline anisotropy is reduced by three orders of magnitude towards a few J/m^3, i.e., small enough to enable superior soft magnetic behavior. Correspondingly the renormalized exchange length, L_{ex}, expands into the μm-regime and, thus, is almost two orders of magnitude larger than the natural exchange length L_0. High resolution Kerr effect studies of nanocrystalline Fe$_{73.5}$Cu$_1$Nb$_3$Si$_{13.5}$B$_9$ indeed reveal very wide domain walls of about 2 μm in thickness indicative of the low effective anisotropy of the material (Schäfer et al. 1991).

If there are no other anisotropies, coercivity and initial permeability are closely related to $\langle K \rangle$ by

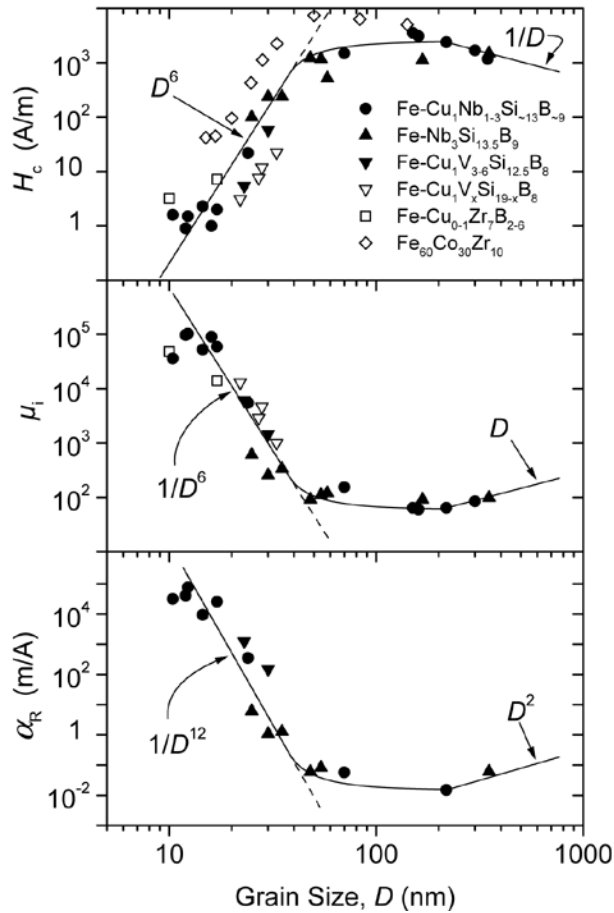$$H_c = p_c \frac{\langle K \rangle}{J_s}; \qquad \mu_i = p_\mu \frac{J_s^2}{\mu_0 \langle K \rangle}, \tag{3.5}$$

Fig. 3.3. Coercivity, H_c, initial permeability, μ_i, and Rayleigh's constant, α_R, of nanocrystalline iron base alloys versus the average grain size. The open symbols are literature data after Sawa and Takahashi 1990 (open down triangles), Suzuki et al. 1991 (open squares) and Guo et al. 1991 (open diamonds).

where J_s is the average saturation magnetization of the material, p_c and p_μ are dimensionless pre-factors close to unity. These relations, obvious for coherent magnetization rotation, in the regime $D \ll L_{ex}$, also apply for domain wall displacements (Herzer 1990) – actually, on the scale of the 10 nm small grains the magnetization vector appears to rotate coherently if a 2 μm ($\approx L_{ex}$) wide domain wall passes by.

3.1.2. Grain size effect
The grain size dependence of the magnetic properties of various nanocrystallized alloy is summarized in fig. 3.3. The predictions of the random anisotropy model seem to provide a good guiding principal through the magnetic properties for grain sizes below about $L_0 \approx 40$–50 nm. Thus, the D^6-dependence is well reflected in the coercivity and the

initial permeability and, similarly, Rayleigh's constant which is proportional to μ_i/H_c behaves like $1/D^{12}$.

If the grain size equals the exchange length the magnetization process is determined by nearly the full magneto-crystalline anisotropy K_1. Accordingly, H_c and $1/\mu_i$ are found to run through a maximum in that grain size regime. Finally, if the grain size exceeds the domain wall width, domains can be formed within the grains and, H_c and $1/\mu_i$ tend to decrease again according to the well known $1/D$-law.

Still, the experimental variation of the grain size for the nanocrystallized material is not completely unambiguous. It inevitably requires changes of the alloy composition and/or the annealing conditions which both changes the volume fraction and composition of the precipitated crystallites and the residual matrix. As a consequence the local magneto-crystalline anisotropy constant, K_1, and the exchange interaction, A, between the grains change simultaneously which causes the broad scatter of the data in fig. 3.3. Thus, for example, the coercivity at comparable grain size is lower in the high Si content alloys than in nanocrystalline Fe(Co)ZrB alloys since Si considerably reduces the magneto-crystalline anisotropy of α-Fe (cf. Gengnagel and Wagner, 1961). Similarly, the higher magneto-crystalline anisotropy of Co signs responsible that nanocrystalline Co-base alloys typically reveal a 5 to 10 times higher coercivity than Fe-base alloys (Hasegawa and Saito 1991) and, hence, are less suited for soft magnetic applications.

Figure 3.4 shows typical hysteresis loops for $D < L_0$. A very characteristic feature in the small grain size regime is the enhancement of the remanence to saturation ratio which is about $J_r/J_s \approx 0.95$ at $D \approx 0.6L_o$ for the one example shown in fig. 3.4. This is another consequence if exchange interaction dominates over the random anisotropies (Chi and Alben 1976). Actually, this possible remanence enhancement by exchange interaction is currently under intensive discussion for novel isotropic, nanoscaled hard magnets (cf. Fukunaga and Inoue 1992).
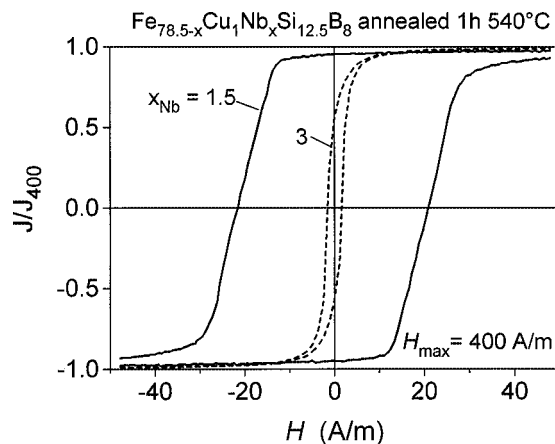

Fig. 3.4. Characteristic hysteresis loops in the nanocrystalline state. The average grain sizes for the examples shown are about 25 nm for $x_{Nb} = 1.5$ at% and 12 nm for $x_{Nb} = 3$ at%, respectively.

Theory predicts the remanence ratio to increase towards $J_r/J_s = 1$ for decreasing grain sizes. Yet at smallest grain sizes, when the random anisotropy is sufficiently washed out, more long-range uniaxial anisotropies take over the control and, as shown in fig. 3.4, the remanence ratio decreases to values around 0.5. Relevant to this are magneto-elastic, creep induced and field induced anisotropies. These additional anisotropies, as schematically indicated in fig. 1.1, limit the benefit of further grain size reduction for permeability and coercivity. The latter is definitely the case in amorphous metals, but also for the high Si content, nanocrystalline $Fe_{bal}Cu_1Nb_3Si$–B alloys, i.e., the further material optimization has to attack magneto-elastic and induced anisotropies. While the magneto-crystalline anisotropy is hardly visible in these optimized alloys, it still seems to limit the magnetic properties of the low Si content Fe–(Nb, Zr)–B alloys.

To summarize, the mechanism of softening in nanocrystalline magnets is basically the same as that for amorphous metals and related to the fact that the structural correlation length is much smaller than the ferromagnetic correlation length. Thus, if the grain size is sufficiently reduced (typically around 10–15 nm) we end up with soft magnetic properties comparable to that of amorphous metals and the general factors for further material optimization are pretty much the same.

3.1.3. Grain coupling

The suppression of magneto-crystalline anisotropy requires that the randomly oriented grains are ferromagnetically coupled by exchange interaction. Consequently, if the exchange interaction is reduced, the local anisotropies will be less effectively averaged out and the soft magnetic properties will degrade.

The crucial role of the exchange interaction becomes most evident from the temperature dependence of the magnetic properties (Herzer 1989) which is shown in fig. 3.5. The exchange interaction between the b.c.c. grains mainly occurs via the interfacial amorphous minority matrix in which the nanocrystallites are embedded. Thus, when the measuring temperature approaches the Curie temperature of the intergranular amorphous phase which is much lower than that of the b.c.c. grains (cf. fig. 2.7), the exchange coupling between the crystallites is largely reduced. As a consequence the initial permeability then drops down by almost two orders of magnitude and the coercivity increases correspondingly. Simultaneously, as shown in fig. 3.6, the domain structure changes from wide domains to a pattern of small, irregular domains (Schäfer et al. 1991). The described behavior is essentially reversible and, thus, obviously not connected with irreversible, microstructural changes during the measurement.

The particular example shown in fig. 3.5 revealed a small uniaxial anisotropy ($K_u \approx 6$ J/m^3) transverse to the ribbon axis induced by magnetic field annealing. In the low temperature regime, this uniaxial, transverse anisotropy is larger than the averaged magneto-crystalline anisotropy, $\langle K_1 \rangle \approx 2$ J/m^3, and, thus, controls the hysteresis loop indicated by the small remanence. However, when approaching T_c^{am}, $\langle K_1 \rangle$ quickly increases due to the reduced grain coupling and takes over the control of the hysteresis loop. This is indicated by the sudden, reversible increase of the remanence to saturation ratio, B_r/B_s, beginning at about 200°C. From random particle theory (Tonge and Wohlfarth 1957, 1958), such a change is expected (i) to start as soon as $K_u/\langle K_1 \rangle < 1$ and (ii) to be largely terminated for $K_u/\langle K_1 \rangle < 0.5$. The B_r/B_s value finally reached at T_c^{am} is not
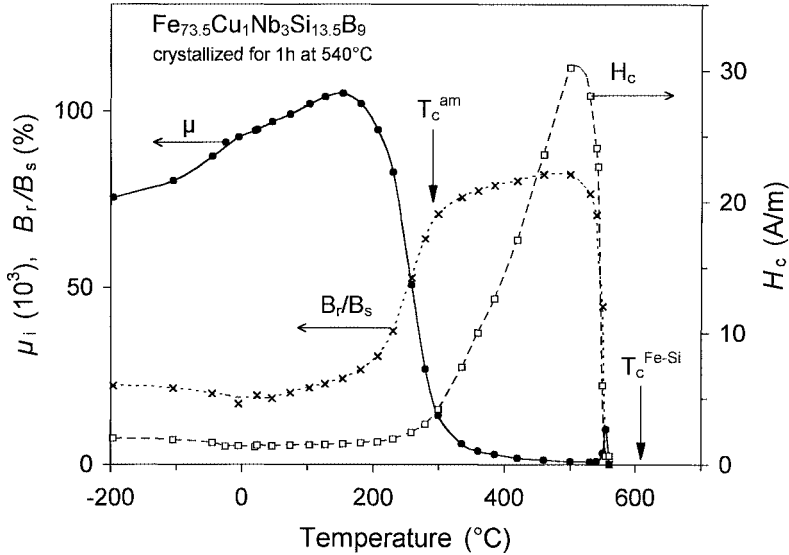
Fig. 3.5. Initial permeability, μ_i, coercivity, H_c, and remanence to saturation ratio, B_r/B_s, of nanocrystalline $Fe_{73.5}Cu_1Nb_3Si_{13.5}B_9$ (annealed 1 h at 540°C + 4 h at 350°C in a transverse magnetic field) versus the measuring temperature (measuring frequency $f = 50$ Hz). The arrows indicates the Curie temperatures of the residual amorphous matrix ($T_c^{am} = 291$°C) and the b.c.c.-grains ($T_c^{FeSi} = 607$°C), respectively.

far from the theoretical value of $B_r/B_s \approx 83\%$ for randomly oriented, non-interacting cubic particles.

With increasing measuring temperature the coercivity reaches a maximum and, finally, decreases towards zero together with the remanent magnetization. Interestingly the latter occurs at a temperature (560°C) below the Curie temperature (607°C), of the b.c.c.-grains. This indicates the transition to superparamagnetic behavior which has been confirmed by a more detailed analysis of Lachowicz and Slawska-Waniewska (1994).

Hernando and Kulik (1994) showed that the maximum of H_c shifts towards T_c^{am}, and that, H_c increases by one order of magnitude as the intergranular distance is increased from $\delta \approx 1$–2 nm to $\delta \approx 5$ nm. Simultaneously the onset temperature, T_0, for superparamagnetic behavior decreases and approximately coincides with T_c^{am} for $\delta \approx 13$ nm.

The whole results for the magnetic behavior above the Curie point, T_c^{am}, of the amorphous matrix indicates that the grain coupling is largely but not completely interrupted above T_c^{am} and still persists to higher temperatures. Yet, the precise coupling mechanism for $T > T_c^{am}$ at present is still under discussion. Both exchange penetration through the thin, paramagnetic intergranular layer (Hernando and Kulik 1994) and dipolar interactions (Herzer 1995a) provide reasonable explanations for interpreting the experimental findings. In any case the strength of the coupling decreases with increasing temperature due to the simultaneous decrease of the magnetization in the b.c.c. grains. Consequently, the soft magnetic properties keep on degrading even above T_c^{am} until thermal energy dominates and the system gets superparamagnetic.
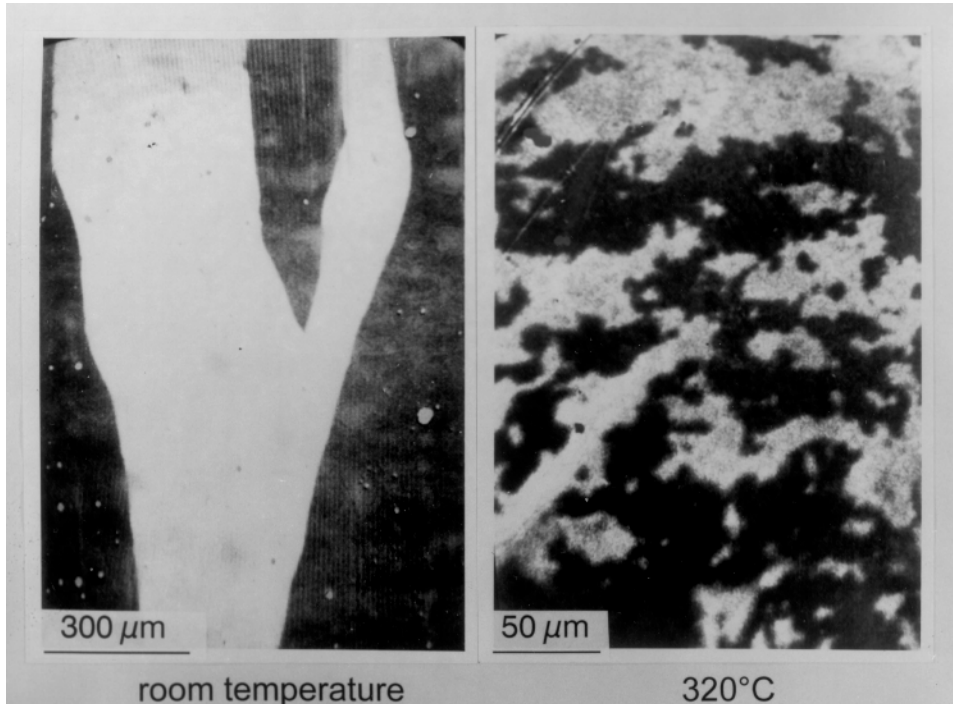
Fig. 3.6. Domain patterns of nanocrystalline $Fe_{73.5}Cu_1Nb_3Si_{13.5}B_9$ (annealed 1 h at $540°C$) at room temperature and at $320°C$, i.e., above the Curie temperature of the residual amorphous matrix (Schäfer, Hubert and Herzer 1991).

The temperature dependence of the magnetic properties demonstrates that it is important to maintain an efficient exchange coupling between the grains by appropriate alloy design such that the Curie temperature of the residual amorphous matrix is clearly higher than application temperatures. Thus, for example, too high additions of Nb (or comparable elements), although favorable for grain refinement, can be disadvantageous because they decrease the Curie temperature of the matrix considerably (Yoshizawa and Yamauchi 1991a). Similarly, reduced grain coupling due to a low Curie temperature of the intergranular phase also provides one of the explanations for the minor soft magnetic properties in nanocrystalline Fe–Zr–B alloys (cf. Slawska-Waniewska et al. 1994) or Fe–Hf–C thin films (Hasegawa et al. 1992).

3.1.4. Hard precipitates
In order to guarantee the magnetic softness of the ultrafine b.c.c. structure, it is still very important to inhibit the formation of Fe–B compounds. Thus, annealing of $Fe_{73.5}Cu_1Nb_3Si_{13.5}B_9$ above $580°C$ leads to the precipitation of Fe_2B with a typical dimension of 50 nm to 100 nm, while the ultrafine grain structure of b.c.c. Fe–Si still persists up to at least $650°C$ (Yoshizawa and Yamauchi 1991b). As already demonstrated

in fig. 2.1, this change of microstructure is accompanied by a severe degradation of the soft magnetic properties.

Domain observations confirm that the ultrafine b.c.c. matrix is effectively hardened by the precipitates although their volume fraction is very small. For samples annealed at 580°C, i.e., in the very initial state of degradation, the domain pattern changes from wide ($\approx 400\,\mu m$) laminar domains to small, only 20 μm wide and irregular domains and the magnetization process is governed by nucleation (Schäfer et al. 1991). The domain size indicates a volume fraction of only a few ppm which is hardly detectable by electron microscopy. The irregular domain pattern scales down by at least two orders of magnitude when the annealing temperature is further increased. At 650°C, finally, when the soft magnetic properties are completely degraded, the intergranular distance between the borides equals about their size (50–100 nm) which corresponds to a small volume fraction of only 10%.

The effective hardening caused by the Fe_2B precipitates already at smallest volume fractions is related to their relatively large size of 50–100 nm and, in particular, to their large magneto-crystalline anisotropy constant, K_1, of about 430 kJ/m^3 (i.e., $L_0 \approx 5$ nm). It is quite instructive to look at the temperature dependence of the magnetic properties of such "overannealed" nanocrystalline materials which is shown in fig. 3.7 together with
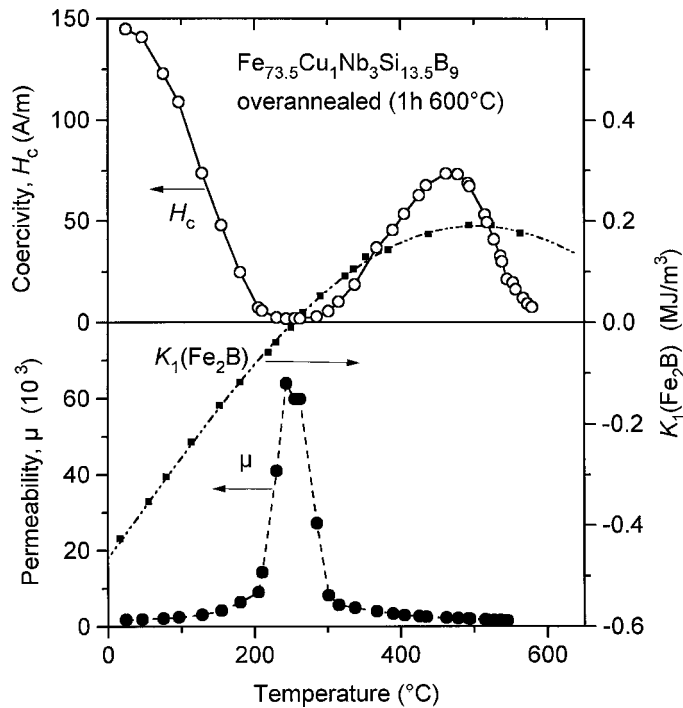

Fig. 3.7. Temperature dependence of coercivity, H_c, and initial permeability, μ_i, of overannealed nanocrystalline $Fe_{73.5}Cu_1Nb_3Si_{13.5}B_9$ with slight traces of Fe_2B, whose magneto-crystalline anisotropy constant K_1 (Iga, Tawara and Yanase 1966) is included in the figure.

the magneto-crystalline anisotropy constant, K_1, of Fe_2B. Thus, the good soft magnetic properties of the nanocrystalline b.c.c. structure are largely recovered when $K_1(Fe_2B)$ passes through zero at $250°C$. This particular temperature dependence allows to detect even smallest amounts of borides hardly visible by more direct structural investigations and, thus, provides a most sensitive tool in order to separate whether an eventual degradation of the soft magnetic properties arises from too large b.c.c. grains or from hard precipitates.

The deleterious impact of small amounts of boride compounds on the soft magnetic properties is in particular visible in alloy compositions with low silicon and correspondingly high boron content (cf. fig. 3.1) even if heat treated in an optimum way. The suppression of the boride compounds by reducing the boron content and by simultaneously alloying more Nb or Zr, thus, results in a considerable improvement of the soft magnetic properties for low Si contents.

3.2. Saturation magnetostriction

The second requirement for excellent soft magnetic properties is the absence of magnetostriction in order to minimize magneto-elastic anisotropies

$$K_\sigma = -\frac{3}{2}\lambda_s\sigma \qquad (3.6)$$

arising from internal or external mechanical stress, σ. For example, even stress relieved toroidal wound cores may still reveal internal stresses of a few MPa. In the amorphous state the material reveals a high positive saturation magnetostriction of $\lambda_s \approx +23 \times 10^{-6}$, typical for Fe-base amorphous alloys. The associated magneto-elastic anisotropy of about $K_\sigma \approx 50$ J/m^3, thus, limits the achievable initial permeability to typically $\mu_i \approx 10^4$.

It is the actual highlight of nanocrystalline Fe-base alloys that the phases formed on crystallization can lead to low or vanishing saturation magnetostriction, λ_s. Figure 3.8 summarizes the situation in the Fe–Cu–Nb–Si–B system. The decrease of λ_s upon the formation of the nanocrystalline state is ultimately responsible for the simultaneous increase of the initial permeability up to more than one order of magnitude (cf. fig. 2.1).

While λ_s is fairly independent of the composition in the amorphous state, it depends sensitively on the Si content in the nanocrystalline state, passing through zero at low and at high Si concentrations around 16 at%. The composition dependence essentially reflects the compositional variation of λ_s found for polycrystalline α-Fe$_{100-x}$Si$_x$ (cf. Yamamoto 1980).

The detailed behavior of λ_s can be understood from the balance of magnetostriction among the structural phases present in the nanocrystalline state, i.e. (Herzer 1991)

$$\lambda_s \approx \nu_{cr}\lambda_s^{FeSi} + (1 - \nu_{cr})\lambda_s^{am}, \qquad (3.7)$$

where λ_s^{FeSi} and λ_s^{am} denote the local magnetostriction constants of the α-Fe–Si grains and the residual amorphous matrix, respectively. As an example, fig. 3.9 shows the decrease of λ_s on annealing in terms of the increasing crystalline volume fraction ν_{cr}.
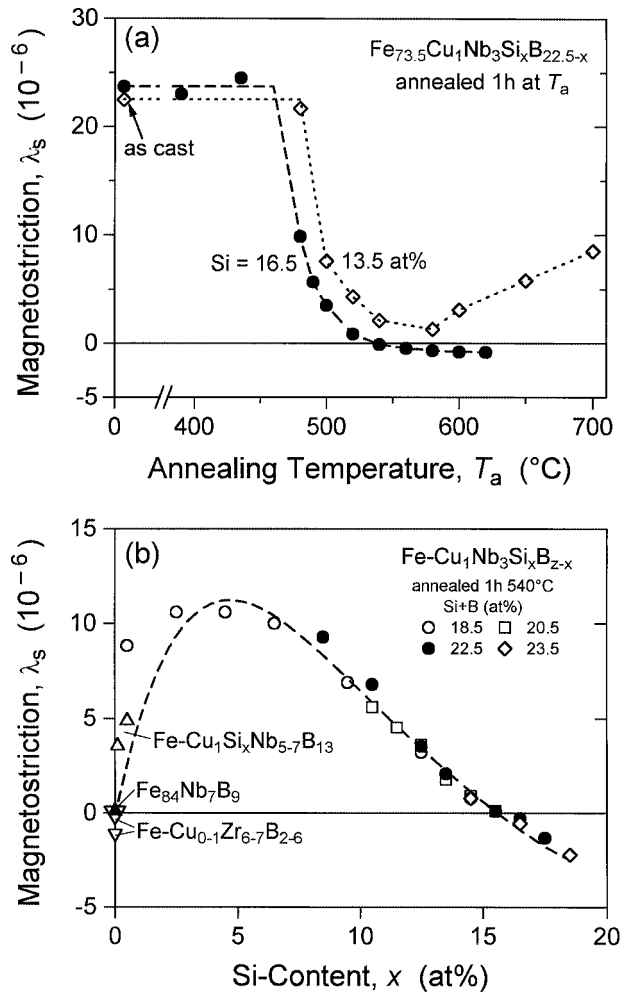
Fig. 3.8. The saturation magnetostriction, λ_s, of Fe–Cu–Nb–Si–B alloys: (a) Influence of the annealing temperature, T_a and (b) influence of the Si content in the nanocrystalline state. The figure includes the data for Fe–Nb–B (solid up triangle) and Fe–(Cu)–Zr–B alloys (open down triangles) from Suzuki et al. 1991, 1993.

Thus, near zero magnetostriction in nanocrystalline Fe-base alloys requires a large crystalline volume fraction with negative magnetostriction in order to compensate the high positive value of the amorphous Fe-based matrix. This is achieved either by a high Si content in the b.c.c. grains ($\lambda_s^{\text{FeSi}} \approx -6 \times 10^{-6}$ for α-Fe$_{80}$Si$_{20}$), like in the Fe–Cu–Nb–Si–B system, or if the grains consist of pure α-Fe ($\lambda_s^{\text{Fe}} \approx -4 \times 10^{-6}$) like in Fe–Zr–B alloys (Suzuki et al. 1991) or Fe–(Si)–Hf–C thin films (Hasegawa et al. 1992). For the low Si content alloys it is further important to have a low boron concentration in order to obtain a large crystalline fraction and to suppress the formation of boride compounds
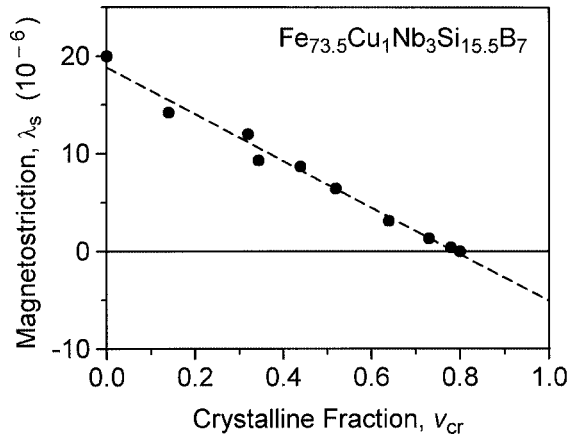
Fig. 3.9. Dependence of the saturation magnetostriction (measured at $50°C$) on the fraction of the precipitated b.c.c.-Fe–Si grains for samples annealed at different temperatures and times (after Twarowski et al. 1995).

which yield a positive contribution to λ_s (cf. the increase of λ_s in fig. 3.8(a) at elevated annealing temperatures where such boride compounds are formed).

An important point to stress is that the superposition of the local magnetostriction constants to zero really results in stress-insensitivity of the magnetic properties like in amorphous Co(Fe)-base alloys. This is again a consequence of the smoothing effect of exchange interaction for structural correlation lengths much smaller than the domain wall width. Thus, the nano-scale fluctuations in magneto-elastic anisotropy associated with the locally varying magnetostrictions are randomly averaged out which results in a single isotropic magnetostriction coefficient. The situation, thus, contrasts with that for large grained crystalline systems, where an average zero saturation magnetostriction does generally not imply stress-insensitivity of the hysteresis loop. Thus, the small grain size is also a decisive factor for the magnetostriction: although it does not directly influence the value of λ_s, it opens a new way to achieve isotropically low magnetostriction by combining the properties of different structural phases with the help of exchange interaction.

The decrease of magnetostriction is the actual reason for the simultaneous increase of the initial permeability upon the formation of the nanocrystalline state. Correspondingly, as shown in fig. 3.1, the soft magnetic properties in the nanocrystalline state improve when the Si content is increased towards the $\lambda_s \approx 0$ composition at 16 at%. Still, the maximum permeability is not necessarily found at the $\lambda_s \approx 0$ line, but at somewhat lower Si contents of around 13 at%. This indicates the presence of further anisotropy contributions increasing towards high Si contents. One explanation is the grain size which is slightly increasing at very high Si contents (Herzer 1991). Another source for the decrease of permeability at higher Si contents are creep induced anisotropies (see next section). For the other $\lambda_s \approx 0$ composition at zero Si content, the benefit of zero magnetostriction is limited by a still noticeable contribution of magneto-crystalline anisotropy.

3.3. Creep induced anisotropies

Mechanical stresses not only cause an anisotropy via magnetostrictive coupling, but being present during annealing can also induce an uniaxial anisotropy due to mechanical creep deformation. The basic features of the creep induced anisotropy in Fe–Cu–Nb–Si–B alloys (Kraus et al. 1992, Herzer 1994a) are fairly the same as they are well known from amorphous alloys (Hilzinger 1981, Nielsen 1985) – no matter whether the anisotropy is induced in the amorphous state, the already nanocrystalline state or during nanocrystallization.

Figure 3.10 shows some typical hysteresis loops after crystallization under tensile stress. The induced anisotropy energy, K_u, is proportional to the tensile stress, σ_{an}, applied during annealing, i.e.,

$$K_u = -\frac{3}{2} k \sigma_{an}, \tag{3.8}$$

whereby the magnetic easy axis is either parallel ($k > 0$) or perpendicular ($k < 0$) to the stress axis. The proportionality constant between K_u and σ_{an} defines the anisotropy parameter k, which is a convenient quantity to characterize the induced anisotropy since it eliminates the explicit stress dependence. Actually, from the way of its definition, k is a kind of fictive magnetostriction constant which would yield an magneto-elastic anisotropy equivalent to K_u if the material was deformed elastically by an applied tensile stress $\sigma = \sigma_{an}$.

Figure 3.11 shows the variation of the creep induced anisotropy parameter, k, with the annealing temperature, T_a and the composition. The decrease of k for $T_a \geqslant 480°C$ coincides with the transformation from the amorphous to the nanocrystalline state which is completed for $T_a \geqslant 500°C$. The creep induced anisotropy in the amorphous state
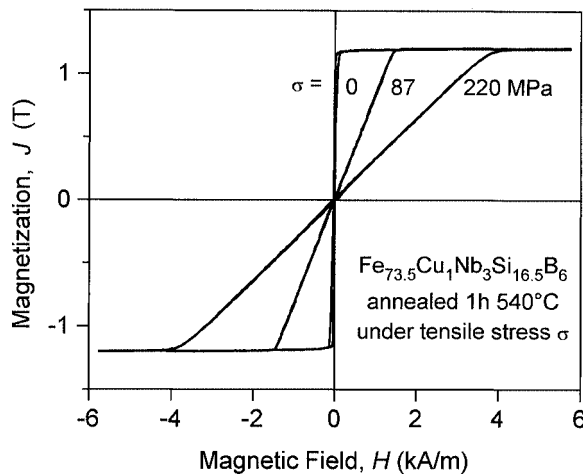

Fig. 3.10. Dc-hysteresis loops of $Fe_{73.5}Cu_1Nb_3Si_{16.5}B_6$ nanocrystallized by annealing for 1 h at 540°C under tensile stress σ.

is comparable to that typically observed in other amorphous alloy systems. However, upon devitrification, its absolute value significantly increases. Within the range where the nanocrystalline state is formed, the anisotropy induced during crystallization is fairly insensitive to the annealing time and temperature and, thus, corresponds to an equilibrium value mainly determined by the Si concentration. In particular, the magnetic hard ribbon axis ($k < 0$) observed for high Si contents turns over to an easy ribbon axis ($k > 0$) for alloys with Si concentration below about 10 at%. An anisotropy of similar order of magnitude can also be induced in samples previously crystallized without stress. However in that case, K_u is more sensitive to the annealing conditions due to a considerably slower kinetics of anisotropy formation.
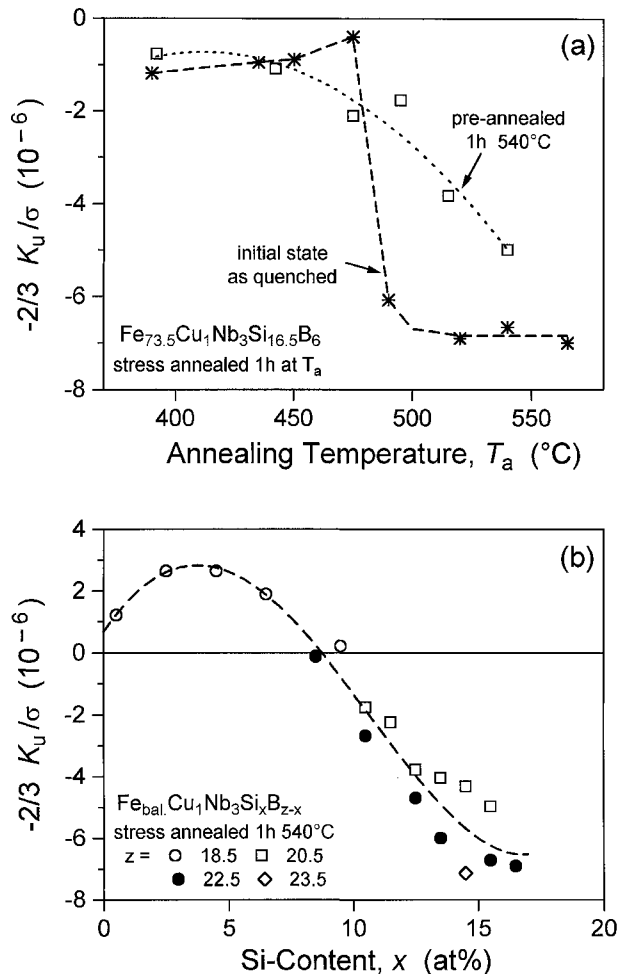

Fig. 3.11. Creep induced anisotropy parameter, $k = -2/3 \cdot K_u/\sigma$, of Fe–Cu–Nb–Si–B alloys: (a) Influence of the annealing conditions and (b) role of the composition in the nanocrystalline state.

The order of magnitude, the variation with annealing temperature or alloy composition, in a way, is similar for both the creep induced anisotropy parameter, k, and the saturation magnetostriction, λ_s, respectively. However, there are also significant differences. In particular, both quantities change sign at different Si concentrations. As a consequence, a strong creep induced anisotropy is found for the near zero magnetostrictive compositions. Thus, although there is a certain analogy in the behavior of k and λ_s, there is no direct correspondence.

The absence of a one to one correlation between creep induced anisotropy and macroscopic magnetostriction is not a particular aspect of the nanocrystalline material but is well known for amorphous alloys (cf. Hilzinger 1981). For the latter Hernando et al. (1985) proposed that the creep induced anisotropy should be related to some local constituents of the magnetostriction coefficients, only, connected to certain types of short range order. Such local magnetostriction contributions clearly exist in the nanocrystalline state and are related to the amorphous matrix and the crystallites. Indeed, the closer analysis of the experimental data (Herzer 1994a) reveals that the strength and orientation of the creep induced anisotropy closely correlates with the local saturation magnetostriction, λ_s^{FeSi}, of the α-FeSi crystallites and can be expressed by

$$K_u \approx -\frac{3}{2} \lambda_s^{\text{FeSi}} \sigma_i \nu_{cr}, \tag{3.9}$$

where λ_s^{FeSi} is the *local* saturation magnetostriction of the b.c.c. Fe–Si grains and ν_{cr} is the crystalline volume fraction. The internal stresses, σ_i, in the crystallites, in the equilibrium case, almost equal to the stress magnitude, σ_{an}, applied during annealing i.e., in this case the anisotropy parameter normalized to the crystalline fraction, k/ν_{cr}, directly corresponds to the the local magnetostriction, λ_s^{FeSi}, of the crystallites.

The likely origin for the internal stresses on the crystallites is *anelastic* creep deformation of the residual amorphous matrix. This yields a bond-orientational anisotropy in the stress free state (Suzuki, Haimovich and Egami 1987). The back stresses due to this polarization of atomic bonds act to increase the dimension along the previous stress axis so that the bond distribution in the amorphous matrix becomes isotropic again. This elongation is finally balanced by the elastic energy of the amorphous matrix and the crystallites.

Thus, the creep induced anisotropy in the nanocrystalline state mainly originates from the magneto-elastic anisotropy of the b.c.c. grains due to tensile back stresses exerted by the anelastically deformed amorphous matrix. The residual amorphous matrix itself gives only a minor contribution to the anisotropy energy. This can be understood from (1) the comparably low magnitude of the creep induced magnetic anisotropy generally observed in amorphous alloys which (2) in the nanocrystalline state is still weighted by the relatively small volume fraction of the amorphous matrix.

Creep-induced anisotropies, in principal, allow to tailor linear hysteresis loops by annealing under controlled tensile stress. However, while this procedure may be applicable for amorphous alloys, the embrittlement upon crystallization practically rules out this possibility for the nanocrystalline material. Actually, the practical impact of creep induced anisotropy in nanocrystalline materials is of more disturbative nature. For example, thin

SiO_2-layers give rise to small tensile stresses during the anneal treatment which yield an unwanted creep induced anisotropy and thus a degradation of the soft magnetic properties even for zero-magnetostrictive compositions (cf. del Real et al. 1994). This is a particular problem for the nanocrystalline material, since its creep induced anisotropy is more than one order of magnitude larger than e.g., in near-zero magnetostrictive, amorphous Co-base alloys. The increase of the absolute value of creep-induced anisotropy towards high Si contents, thus, is able to explain the simultaneous decrease of permeability (fig. 3.1) although the magnetostriction passes through zero. This decrease of permeability is accompanied by a decrease of the remanence to saturation ratio indicative of disturbative uniaxial anisotropies transverse to the ribbon axis. The low remanence ratio further indicates that the degradation of the soft magnetic properties is not primarily caused by magneto-crystalline anisotropy due to the slightly increasing grain size since this would yield a remanence enhancement.

3.4. Magnetic field induced anisotropies

So far magnetic anisotropies have been discussed as a rather disturbative factor for the soft magnetic properties. However, if properly controlled, they also can be a powerful tool in order to tailor the shape of the hysteresis loop according to the demands of various applications. Like in other soft magnetic materials this can be realized by magnetic field annealing, which induces a uniaxial anisotropy with an easy axis parallel to the direction of the magnetic field applied during the heat treatment. Some typical examples are shown in fig. 3.12.

The almost perfect rectangular or flat shaped hysteresis loops obtained after field annealing indicate that the field induced anisotropy clearly dominates over the other anisotropy contributions, including the magneto-crystalline anisotropy. Still, the induced anisotropy constant, K_u, can be tailored small enough in order to achieve highest permeabilities (for example, $K_u \approx 6$ J/m^3 and $\mu \approx 100\,000$ as for the F1 loop shown in fig. 3.12).

The *flat shaped* loops (F1, F2) are obtained by transverse field annealing, i.e., by inducing a uniaxial anisotropy perpendicular to the ribbon axis. The magnetization process is determined by rotation of the magnetization vectors from the easy direction towards the ribbon axis. This results in a permeability, μ, practically constant up to ferromagnetic saturation which by

$$\mu = J_s^2/(2\mu_0\,K_u) \tag{3.10}$$

is directly related to the induced anisotropy energy constant, K_u.

The *rectangular* loop (Z) results after longitudinal field annealing. The uniaxial anisotropy is parallel to the ribbon axis and, thus, the magnetization process is dominated by $180°$ domain wall displacements. Highest maximum permeabilities can be achieved this way. Since the domain wall energy is proportional to the square root of K_u, low induced anisotropies in this case facilitate domain refinement which results in good dynamic properties like, e.g., reduced anomalous eddy current losses.
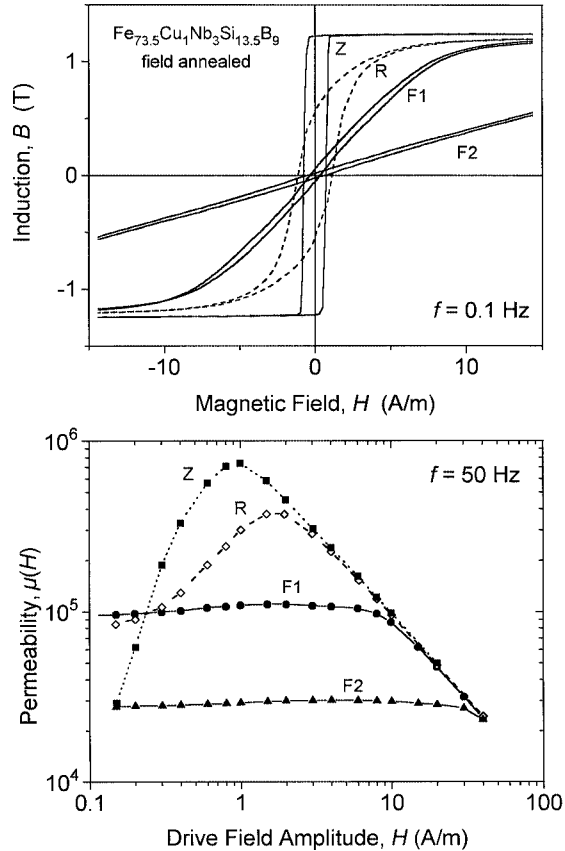
Fig. 3.12. Quasistatic hysteresis loops and 50 Hz permeability of nanocrystalline $Fe_{73.5}Cu_1Nb_3Si_{13.5}B_9$ annealed for 1 h at $540°C$ without (R) and with a magnetic field applied parallel (Z) and transverse (F2; $K_u \approx 20$ J/m^3, $\mu \approx 30 \times 10^3$) to the magnetic path. Sample F1 ($K_u \approx 6$ J/m^3, $\mu \approx 100 \times 10^3$) was first crystallized at $540°C$ and subsequently transverse field annealed at $350°C$.

The *round* loop (R) results after conventional annealing without magnetic field. This, however, does not mean that there are no induced anisotropies. The latter are always induced along the direction of the local spontaneous magnetization within a ferromagnetic domain as long the annealing temperature is lower than Curie temperature. A ferromagnetically saturating magnetic field just induces a uniform anisotropy. Thus, the heat treatment without field produces a random distribution of uniaxial anisotropies induced parallel to the magnetization vector in each domain. The remanence to saturation ratio of around 50%, typical for randomly oriented uniaxial anisotropies, indicates that these randomly induced anisotropies fluctuate on a scale larger than the exchange length and effectively contribute to the hysteresis loop. The magnetization process is a mixture of magnetization rotation and domain wall displacements. Characteristics features of the round loop are a high initial and high maximum permeability.
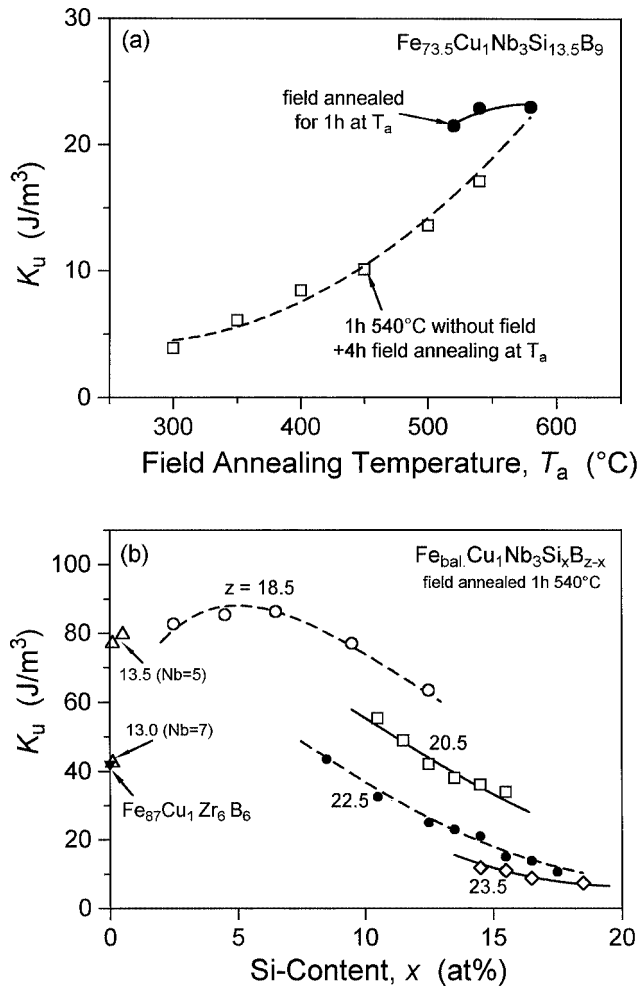
Fig. 3.13. Field induced anisotropy, K_u, in nanocrystalline Fe–Cu–Nb–Si–B alloys: (a) Influence of the annealing conditions and (b) role of the composition in the nanocrystalline state.

The field annealed samples mostly reveal a smaller coercivity than the samples annealed without field which can be understood from the more simple domain configuration due to the uniform induced anisotropy. Correspondingly, proper transverse field annealing allows higher initial permeabilities than obtained by the conventional heat treatment and as shown in fig. 3.1. It, hence, extends the range of highest initial permeabilities towards higher Si-concentrations, in particular towards the $\lambda_s \approx 0$ composition.

The tremendous practical impact of field-induced anisotropies is almost self-evident. The understanding of the induced anisotropy energy is, thus, lastly the key for the reproducible control of the soft magnetic properties. The magnitude of K_u generally de-

pends upon the annealing conditions (Yoshizawa and Yamauchi 1990b) and on the alloy composition (Herzer 1994b). Figure 3.13 summarizes the situation in nanocrystalline Fe–Cu–Nb–Si–B alloys annealed in a transverse magnetic field.

If the material is nanocrystallized first without applied field and subsequently field annealed at lower temperatures, the resulting induced anisotropy depends sensitively on the field annealing temperature, T_a, and the annealing time, t_a. Still, this dependency is insensitive enough to make use of the annealing conditions in order to tailor the desired level of permeability as exemplified by the F1- and F2-loops shown in fig. 3.12. Lowest induced anisotropies, i.e., highest permeabilities can be achieved this way.

If the field annealing is performed during nanocrystallization, the induced anisotropy reaches a maximum value which is relatively insensitive to the precise annealing conditions and, thus, corresponds to the equilibrium value characteristic for the alloy composition. The most prominent influence of the alloy composition hereby arises from the silicon and boron contents. The induced anisotropy energy decreases with increasing metalloid contents and, in particular, with increasing Si/(Si+B) ratio. Accordingly, the lowest anisotropy energies and, thus, the highest permeabilities are found for the high Si content alloys. The effect of the copper and niobium concentration on K_u is only minor as long as both elements are chosen such that a homogeneous nanocrystalline structure is formed. However, the influence of niobium or other refractory elements on K_u is fairly significant when its concentration is critical in order to obtain a fine, homogeneous grain structure. This is in particular the case for the alloy compositions with very low silicon and correspondingly high boron contents. Such compositions tend to reveal traces of boride compounds and may also have larger, inhomogeneous b.c.c. grains.

The anisotropy induced during nanocrystallization in a magnetic field primarily originates from the b.c.c. grains (Herzer 1994b, 1995b). The reason simply is that magnetic field annealing can only induce a magnetic anisotropy if the annealing temperature is below the Curie temperature, T_c. Thus, the typical annealing temperature of 540°C is below the T_c of the b.c.c. grains (600°C to 750°C), but clearly above the T_c of the amorphous matrix (200°C to 400°C).

Consequently, the macroscopic anisotropy K_u, the anisotropy locally induced in the b.c.c. grains, i.e., K_u^{FeSi}, and the crystalline fraction, ν_{cr}, should be related by

$$K_u = \nu_{cr} K_u^{FeSi}, \tag{3.11}$$

provided no further high T_c-phases, like, e.g., boride compounds, are present. Accordingly, K_u/ν_{cr} has been plotted versus the Si content of the b.c.c. grains in fig. 3.14. This representation rearranges most of the anisotropy data on a single line and, thus, brings about a considerably clearer view of the alloying effect. Thus, the induced anisotropy in nanocrystalline Fe–Cu–Nb–Si–B alloys is mainly determined by the Si content and the fraction of the b.c.c. grains. The dependence of K_u/ν_{cr} on the Si content in the b.c.c. grains is comparable with that observed for conventional α-FeSi single crystals (Sixtus 1962, 1970) where the formation of the field induced anisotropy has been proposed to arise from the directional ordering of Si-atom pairs.

The decrease of K_u with increasing Si content, in terms of Néel's (1954) theory, can be related to the formation of a DO_3 superlattice structure for Si-concentrations above
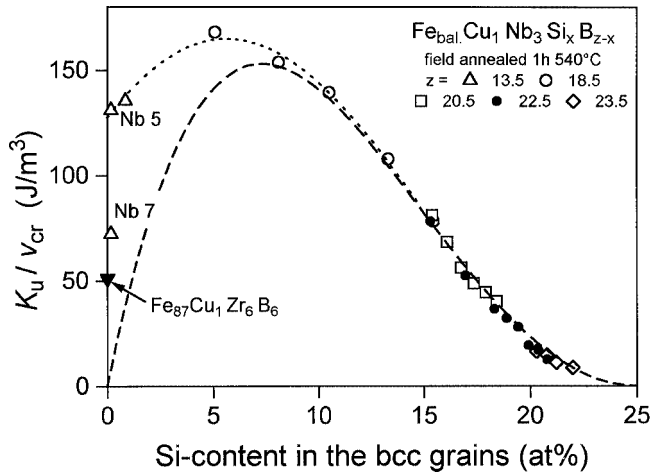
Fig. 3.14. Field induced anisotropy, K_u, normalized to the crystalline fraction, ν_{cr}, as a function of the Si content in the α-FeSi grains of nanocrystalline Fe–Cu–Nb–Si–B alloys. The dashed line is a fit to the high Si content alloys according to eq. (3.12) with $K_o = 612$ J/m^3.

about 10 at%. For completely ordered Fe$_3$Si, the lattice sites for the Fe and Si atoms are entirely determined by chemical interactions, allowing no degree of freedom for an orientational order. However, for a composition Fe$_{1-y}$Si$_y$ with less than 25 at% Si no complete DO$_3$ order can be reached and Fe atoms will occupy the vacant sites in the Si sublattice. The way the latter is done provides the necessary degrees of freedom for an orientational order. Thus, the present anisotropy data above about 10 at% Si can be well described by

$$K_u/\nu_{cr} = K_o c^2 (1 - c^2), \tag{3.12}$$

where $c = (1 - 4y)$ denotes the fractional concentration of Fe at Si sites (see dashed line in fig. 3.14). The low K_u-level due to the superlattice structure at higher Si contents is an additional key factor for the high initial permeabilities which can be achieved in these alloys despite their high Curie temperature and their high saturation induction.

For low Si contents, the situation is more complex and still under investigation. Pure α-Fe should reveal no field induced anisotropy in accordance with the decrease of K_u reported for α-FeSi single crystals towards low Si contents (Sixtus 1962, 1970). However, the nanocrystalline alloys still shows a considerable amount of induced anisotropy at vanishing Si contents. This indicates (1) that the crystallites do not consist of pure α-Fe or (2) the presence of other high T_c-phases, like Fe$_3$B ($T_c \approx 550°$C) or Fe$_2$B ($T_c \approx 740°$C) compounds which may significantly contribute to K_u. The latter is supported by the decrease of K_u upon reducing the boron content and increasing the Nb or Zr content which, as discussed before, suppresses the formation of such compounds.

4. Application oriented properties

Low effective magnetocrystalline anisotropy and low or vanishing magnetostriction are the key to superior soft magnetic properties. There are only a few alloy compositions that exhibit this combination of properties: the permalloys, Sendust, manganese–zinc ferrites, the amorphous cobalt-based alloys and, the nanocrystalline iron-based alloys. As exemplified in fig. 4.1, however, among these materials, the nanocrystalline alloys offer the highest saturation induction, B_s, and, simultaneously, the highest level of permeability, μ. Typical commercial grades by now available under the tradenames FINEMET$^{\circledR}$ (Hitachi Metals Ltd. 1993) and VITROPERM$^{\circledR}$ (Vacuumschmelze GmbH 1993) are located at the compositions $Fe_{\sim 74}Cu_1Nb_3Si_{13-16}B_{6-9}$ and offer a saturation induction of typically $B_s = 1.2$–1.3 T and initial permeabilities up to $\mu_i \approx 150 \times 10^3$.

Of course, soft magnetic applications not only require highest permeability and lowest coercivity. A well defined shape of the hysteresis loop with not necessarily highest but a well defined level of permeability adjusted to the particular application is as important. As discussed before this is managed by magnetic field annealing which allows to tailor a wide range of properties. The flat type hysteresis loops (cf. fig. 3.12) have proven to be particularly useful in a series of applications and, therefore, will be highlighted in the following. The level of permeability can be varied from about $\mu_i \approx 30 \times 10^3$ (e.g., VITROPERM$^{\circledR}$ 500F, FINEMET$^{\circledR}$ FT3-L) to about 100×10^3 (e.g., VITROPERM$^{\circledR}$ 800F). Highest permeabilities are required for magnetic cores in ground fault interrupters or common mode chokes. Applications where a lower permeability level is more suitable are, for example, magnetic cores for high frequency power transformers in switched power supplies or for interface transformers in the ISDN-telecommunication network.
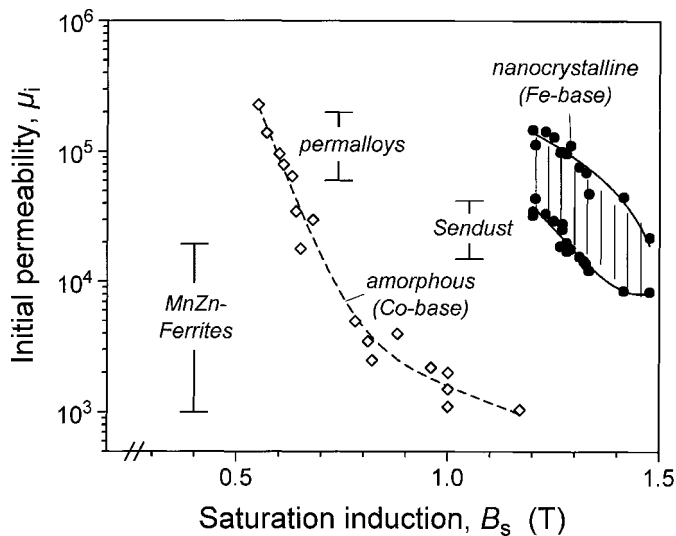

Fig. 4.1. Typical initial permeabilities and saturation inductions for low magnetostrictive, soft magnetic materials.

Low losses, good high frequency behavior, favorable temperature dependence and high thermal stability of the soft magnetic properties are further requirements for most applications. We will discuss in more detail below these more general demands which as well are advantageously fulfilled by the nanocrystalline alloys.

The only draw-back of the nanocrystalline material seems to be the severe embrittlement upon crystallization which requires final shape annealing and restricts their application mainly to toroidally wound cores.

4.1. High frequency behavior and losses

Figure 4.2 gives an example of the frequency dependence of the absolute value of complex permeability and its imaginary part μ'' in terms of the relative loss factor $\mu''/|\mu|^2$. The latter is directly related to the cycle losses at constant induction amplitude B by

$$\frac{P}{f} = \frac{\pi B^2 \mu''}{\mu_0 |\mu|^2}. \tag{4.1}$$

The core losses are compared in fig. 4.3 with those of other soft magnetic materials. Accordingly, the frequency dependence of permeability and the core losses of the nanocrystalline FeCuNbSiB alloys are comparable to those of amorphous Co-based alloys and surpass by far the properties of conventional materials, even that of ferrites, over the whole frequency range up to several 100 kHz. The data given here are for the flat type hysteresis loops. Such low remanence ratio materials generally show the best dynamic properties due to the homogeneous change of magnetization by rotation and can
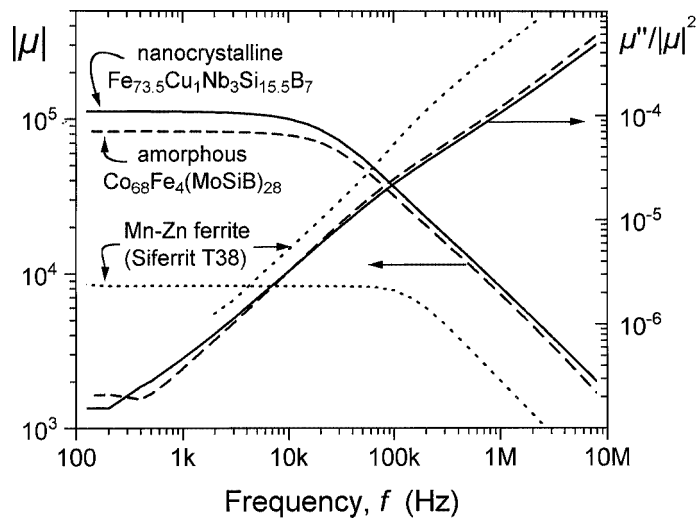

Fig. 4.2. Frequency dependence of permeability, $|\mu|$, and the relative loss factor, $\mu''/|\mu|^2$, for nanocrystalline $Fe_{73.5}Cu_1Nb_3Si_{15.5}B_7$ and comparable, low remanence soft magnetic materials used for common mode choke cores.

be well described by classical eddy current loss theory. High remanence loops, where the magnetization process is determined by domain wall displacements, show up higher losses (typically twice to three times) due to "anomalous" eddy current contributions. Still, this is generally the case for all materials and, in comparison, the nanocrystalline and Co-based amorphous alloys again behave advantageously (Yoshizawa and Yamauchi 1989).

The favorable high frequency behavior is essentially related to (1) the thin ribbon gauge of $d \approx 20\,\mu m$ inherent to the production technique and (2) to a relatively high electrical resistivity of typically $\rho \approx 115\,\mu\Omega\,cm$ related to the high Si content in the b.c.c. grains (cf. Bozorth 1951) and the intergranular amorphous phase. Both parameters are comparable to amorphous metals and yield low eddy current losses, P_e, which in thin sheets at a frequency f and a induction level B are given per volume by (cf. Kupfmüller 1990 or other textbooks)

$$P_e = \frac{3}{x}\frac{\sinh x - \sin x}{\cosh x - \cos x}\frac{(\pi d f B)^2}{6\rho} \underset{x\ll 1}{\approx} \frac{(\pi d f B)^2}{6\rho} \tag{4.2a}$$

with $x = 2\sqrt{f/f_W}$, where

$$f_W = \frac{4\rho}{\pi\mu_0\mu_i d^2} \tag{4.2b}$$

is the limiting frequency above which the exciting magnetic field no longer fully penetrates the specimen and, accordingly, the permeability decreases as a function of the frequency (cf. fig. 4.2). The low coercivity of typically $H_c < 0.5$–1 A/m furthermore
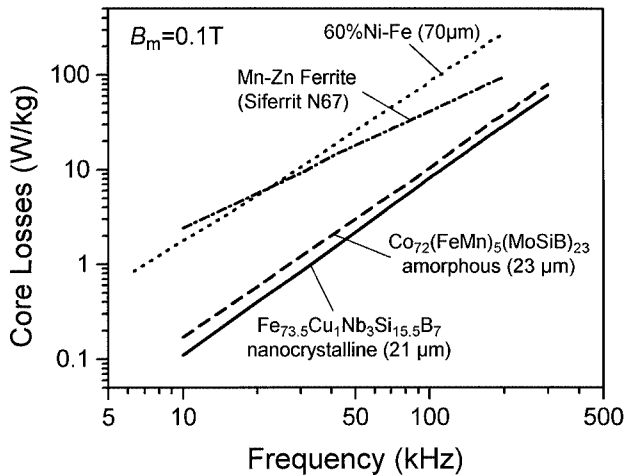

Fig. 4.3. Core losses vs. frequency for nanocrystalline $Fe_{73.5}Cu_1Nb_3Si_{15.5}B_7$ and other low remanence, soft magnetic materials used for high frequency power transformers.

minimizes the contribution of hysteresis loss and, thus, also guarantees lowest total losses at line frequency and below.

4.2. Temperature dependence of the magnetic properties

The temperature dependence of the permeability is shown fig. 4.4 in comparison with other materials. In highly permeable crystalline alloys, like permalloy (80% NiFe), the magnetocrystalline anisotropy constant K_1 is adjusted to zero by alloying and annealing which, however, is effective only for a certain temperature. Thus, the temperature dependence of K_1 yields a pronounced variation of the soft magnetic properties around the temperature where K_1 is zero (cf. Pfeifer 1992). In particular, the drop of permeability towards lower temperatures (because of $K_1 > 0$) can be a problem for certain applications like, e.g., magnetic cores for ground fault interrupters. In comparison, in nanocrystalline and amorphous materials the magnetocrystalline anisotropy is averaged out by exchange interaction which is effective over a large temperature range. Accordingly the magnetic properties vary smoothly in both materials. In amorphous alloys the behavior is mainly determined by induced anisotropies whose magnitude decreases and, thus, the permeability typically increases with increasing temperature. The situation is somewhat more complex in nanocrystalline materials. While in soft magnetic amorphous alloys the contribution of the random atomic scale anisotropies is totally negligible, this is not the case in nanocrystalline materials due to the larger structural correlation length. Thus, as discussed in section 3.1.2, the soft magnetic properties tend to degrade towards higher temperatures since the intergranular exchange coupling is reduced (cf. fig. 3.5). At application temperatures, this mechanism typically causes a smooth decrease of permeability with increasing temperature (cf. Yoshizawa and Yamauchi 1991a). This decrease,
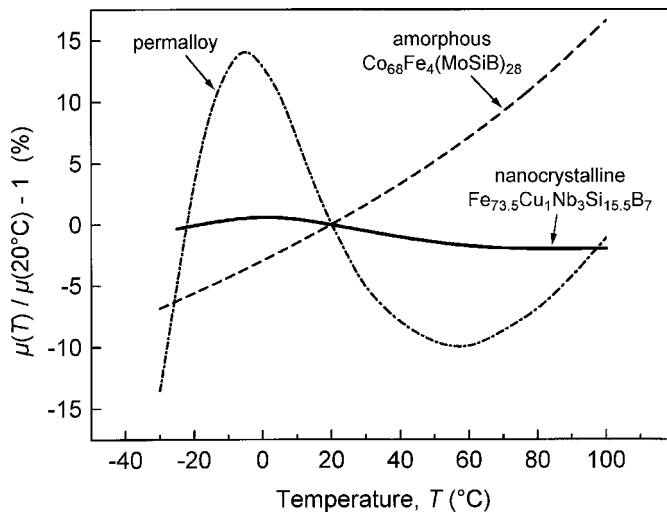

Fig. 4.4. Relative change of the initial permeability normalized to its room temperature value vs. the typical range of application temperatures for comparable, highly permeable soft magnetic materials.
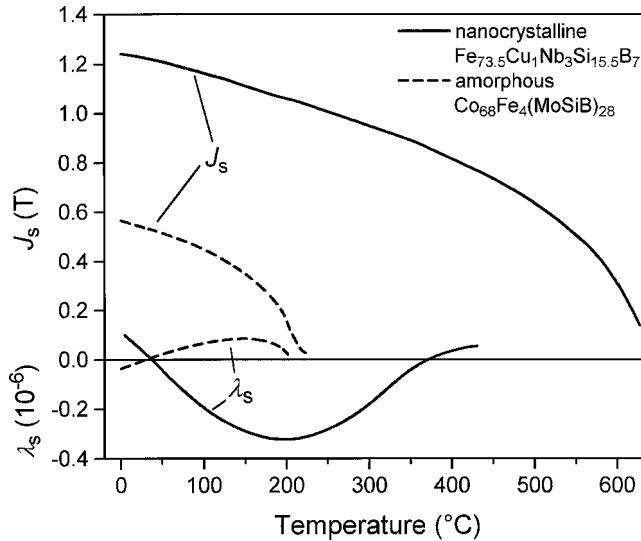
Fig. 4.5. Temperature dependence of the saturation magnetization, J_s, and the saturation magnetostriction, λ_s, of nanocrystalline $Fe_{73.5}Cu_1Nb_3Si_{15.5}B_7$ (full lines) and a comparable, highly permeable amorphous Co-based alloy (dashed lines).

however, can be compensated by appropriate choice of the annealing conditions and the alloy composition. Thus, as exemplified in fig. 4.4, it is possible to adjust an almost negligible temperature dependence of permeability over the whole range of typical application temperatures – the physical mechanism is still under investigation.

Figure 4.5, finally, complements the temperature dependence of saturation magnetization and saturation magnetostriction of the near-zero magnetostrictive $Fe_{73.5}Cu_1Nb_3$-$Si_{15.5}B_7$ composition. The magnetostriction passes through zero near room temperature. Its temperature variation around $\lambda_s = 0$ is stronger than in near-zero magnetostrictive amorphous Co-based alloys. Still, the magnetostriction of the nanocrystalline alloy can be kept as small as $|\lambda_s| < 0.2 \times 10^{-6}$ over the whole range of typical application temperatures.

4.3. Thermal stability

Long-term thermal stability of the magnetic properties is a further requirement for application, in particular at elevated operation temperatures. Empirically, thermally induced aging of the magnetic properties is the more critical the better these properties are. Apart from temperature and time, the aging behavior also depends on the magnetizing conditions during operation whose limiting cases are the remanent (or demagnetized) state and the ferromagnetically saturated state, respectively. The latter generally represents the worst case. Figure 4.6 compares the aging behavior of nanocrystalline $Fe_{73.5}Cu_1Nb_3Si_{15.5}B_7$ with flat type hysteresis loop with that of other highly permeable materials. The thermal stability of the nanocrystalline material surpasses by far that of
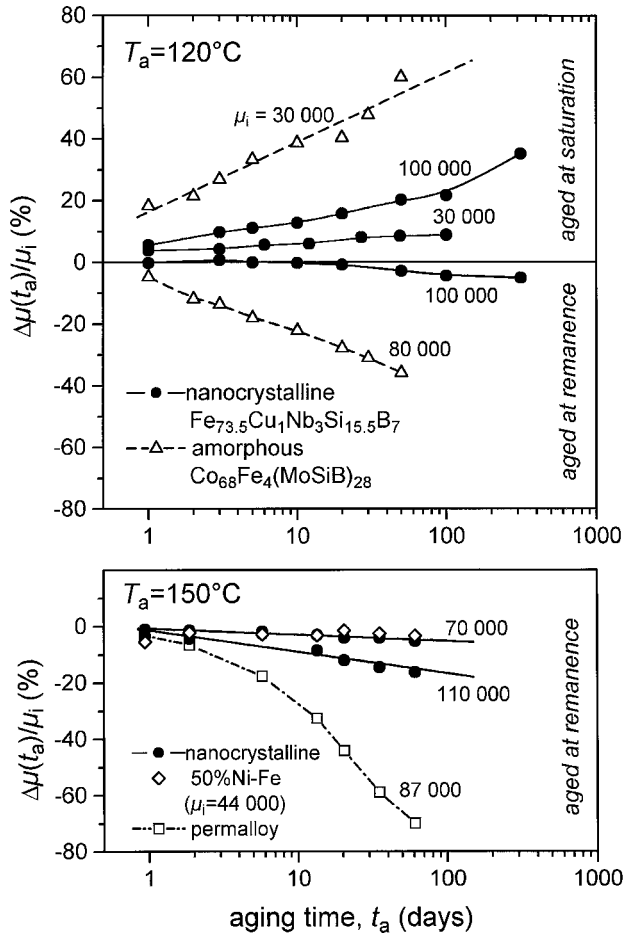
Fig. 4.6. Relative change of the initial permeability of vs. the time of thermal aging at elevated temperatures. The comparison is made for materials with low remanence hysteresis loops.

amorphous alloys and even that of permalloys. This allows higher continuous service temperatures up to 150°C.

The mechanisms of thermal aging, in principal, are the same as those which are used to tailor the magnetic properties during annealing but at a reduced kinetics due to the comparably lower operation temperature. A dominant contribution arises from the formation of locally field induced uniaxial anisotropy along the spontaneous magnetization vectors within the ferromagnetic domains. This explains, for example, the distinct aging behavior for different magnetizing conditions. During aging at remanence the magnetization is aligned parallel to the anisotropy axis which increases the magnitude of the induced anisotropy and, thus, decreases the permeability. Aging at saturation induces a longitudinal anisotropy which reduces the transverse anisotropies and, hence, first in-

creases the permeability and, finally, changes the loop characteristics from a linear, flat type to a square loop.

The excellent thermal stability of the magnetic properties in nanocrystalline alloys is closely related to the factors governing the anisotropy formation discussed in section 3.4. Thus, the reduced degrees of freedom for anisotropy formation due to the superlattice structure together with the high Curie temperature allow to stabilize very small induced anisotropies and, hence, high permeabilities at annealing temperatures much higher than it is possible for highly permeable amorphous alloys or permalloy. This essentially reduces the kinetics for anisotropy changes at application temperatures. In comparison with amorphous metals, the thermal stability is additionally improved by the more stable crystalline structure.

5. Conclusions

Nanocrystalline Fe based alloys combine the advantageous properties of various soft magnetic materials, i.e., the high saturation induction of Fe-based alloys, the high permeability and low magnetostriction of permalloys or amorphous Co-based alloys and the favorable high frequency behavior of ferrites or amorphous metals.

The key to this property combination is the structural correlation length which is much smaller than the ferromagnetic correlation length. Thus, like in amorphous metals, the magneto-crystalline anisotropy is randomly averaged out by exchange interaction. But at the same time the averaging effect of exchange interaction in the small grain size regime allows to combine the individual properties of different structural phases which expands the variability of property tailoring over that of alloying single phases. The isotropically low or vanishing magnetostriction which can be achieved in this new way is a particular example.

The most superior soft magnetic properties are found for the original compositions around $Fe_{\sim 74}Cu_1Nb_3Si_{13-16}B_{6-9}$ and are comparable to the excellent properties known so far from permalloys or Co-base amorphous alloys. The advantages, however, are the higher saturation induction of 1.2–1.3 T and a significantly better thermal stability of the soft magnetic properties. The material is meanwhile offered commercially with a wide range of properties appropriate for various applications. The combination of high saturation magnetization, high permeability, good frequency behavior, low losses and the good thermal stability allows the reduction of size and weight of magnetic components used in, for example, switched mode power supplies or telecommunication. Apart from its technical performance the material is based on the inexpensive raw materials iron and silicon. The amorphous pre-cursor material of the Fe–Cu–Nb–Si–B alloys furthermore is easily accessible by rapid solidification from the melt – a well established technique for large scale production of amorphous metals. All together has led to a steadily increasing application of the new material in magnetic cores for ground fault interrupters, common mode chokes and high frequency transformers.

A second family of near-zero magnetostrictive, nanocrystalline alloys are based on $Fe_{\sim 84-91}(Cu_1)–(Zr, Nb)_{\sim 7}B_{2-9}$ and exhibit a still higher saturation magnetization up to 1.7 Tesla. The soft magnetic properties are comparable to those of crystalline 50–60% Ni–Fe or amorphous Fe-base alloys but combined with low magnetostriction and

lower losses. These alloys and derivatives are currently still under intensive research. Their major draw-back is a lower glass forming ability and/or castability due to the oxygen reactivity of the Zr addition. Thus, these alloys presently are still restricted to the laboratory scale, since they require a by far more sophisticated production technology than the more conventional Fe–Si–B compositions.

Thin film and multilayering technique allow to prepare and to combine a still wider range of alloy compositions and different structural phases and, thus, provide a huge potential to expand considerably the accessible property spectrum of nanocrystalline systems in particular for future high-frequency devices, e.g., for magnetic recording.

Apart from their technical impact the nanocrystalline materials offer a fascinating system to study magnetic interactions. Thus, for example, they combine even within a single sample a variety of phenomena ranging from soft, over hard to finally superparamagnetic behavior.

References

Alben, R., J.J. Becker and M.C. Chi, 1978, J. Appl. Phys. **49**, 1653.

Arai, K., I. Tsutsumitakae and K. Ohmori, 1984, IEEE Trans. Magn. **MAG-20**, 1463.

Ayers, J.D., V.G. Harris, J.A. Sprague and W.T. Elan, 1994, Appl. Phys. Lett. **64**, 974.

Birringer, R. and H. Gleiter, 1988, Encyclopedia of Materials Sciences and Engineering, ed. W. Cahn (Pergamon Press) Suppl. 1, p. 339.

Bozorth, R., 1951, Ferromagnetism (D. van Nostrand, Princeton, N.J.) p. 76.

Chi, M.C. and R. Alben, 1976, AIP Conf. Proc. **34**, 316.

Chudnovsky, E.M., W.M. Saslow and R.A. Serota, 1986, Phys. Rev. B **33**, 251.

del Real, R.P., C. Prados, F. Conde and A. Hernando, 1994, J. Magn. Magn. Mater. **131**, 183.

Fukunaga, H., and H. Inoue, 1992, Jpn. J. Apl. Phys. **31**, 1347.

Fujimori, H., 1995, Scr. Metall. Mater. **33**, 1625.

Gengnagel, H., and H. Wagner, 1961, Z. Angew. Phys. **8**, 174.

Guo, H.-Q., T. Reininger, H. Kronmüller, M. Rapp and V.Kh. Skumrev, 1991, Phys. Status Solidi A **127**, 519.

Hampel, G., A. Pundt and J. Hesse, 1992, J. Phys.: Cond. Matter **4**, 3195.

Hasegawa, N., and M. Saito, 1991, in: Proc. of Int. Symp. on 3d Transition–Semi Metal Thin Films, Magnetism and Processing (Japan Soc. for the Promotion of Science, 131 Committee, Sendai, Japan) p. 165.

Hasegawa, R., V.R.V. Ramanan and G.E. Fish, 1982, J. Appl. Phys. **53**, 2276.

Hasegawa, N., N. Kataoka and H. Fujimori, 1992, IEEE Transl. J. Magn. **7**, 880 (in Japanese).

Hasegawa, N., M. Saito, N. Kataoka and H. Fujimori, 1993, J. Mater. Eng. Perform. **2**, 181.

Hernando, A., and T. Kulik, 1994, Phys. Rev. B **49**, 7064.

Hernando, A., V. Madurga, J.M. Barandiarán and O.V. Nielsen, 1985, Solid State Commun. **54**, 1059.

Herzer, G., 1989, IEEE Trans. Magn. **MAG-25**, 3327.

Herzer, G., 1990, IEEE Trans. Magn. **MAG-26**, 1397.

Herzer, G., 1991, in: Proc. of Int. Symp. on 3d Transition–Semi Metal Thin Films, Magnetism and Processing (Japan Soc. for the Promotion of Science, 131 Committee, Sendai, Japan) p. 130.

Herzer, G., 1993, Phys. Scr. T **49**, 307.

Herzer, G., 1994a, IEEE Trans. Magn. **MAG-30**, 4800.

Herzer, G., 1994b, Mater. Sci. Eng. A **181**–**182**, 876.

Herzer, G., 1995a, Scr. Metall. Mater. **33**, 1741.

Herzer, G., 1995b, Nanostructured and Non-Crystalline Materials, eds M. Vazquez and A. Hernando (World Scientific, Singapore) p. 449.

Herzer, G., and H.R. Hilzinger, 1986, J. Magn. Magn. Mater. **62**, 143.

Herzer, G., and H. Warlimont, 1992, Nanostruct. Mater. **1**, 263.

Hilzinger, H.R., 1981, in: Proc. 4th Int. Conf. on Rapidly Quenched Metals (Sendai) p. 791.

Hitachi Metals Ltd., 1993, New materials from the nano-world. Magnetic Cores, Data sheet Y-930415.

Hono, K., and T. Sakurai, 1995, Appl. Surf. Sci. **87–88**, 166.

Hono, K., K. Hiraga, Q. Wang, A. Inoue and T. Sakurai, 1992, Acta Metall. Mater. **40**, 2137.

Iga, A., Y. Tawara and A. Yanase, 1966, J. Phys. Soc. Jpn **21**, 404.

Inoue, A., K. Kobayashi, J. Kaneira and T. Masumoto, 1981, Sci. Rep. Res. Inst. Tohoku Univ. A **29**, 331.

Kataoka, N., T. Matsunaga, A. Inoue and T. Masumoto, 1989, Mater. Trans. JIM **30**, 947.

Kneller, E.F. and H. Hawig, 1991, IEEE Trans. Magn. **27**, 3588.

Kneller, E.F., 1969, Magnetism and Metallurgy, eds. A.E. Berkowitz and E. Kneller (Academic Press, New York, London) p. 365.

Köster, U., U. Schönemann, M. Blank-Bewersdorff, S. Brauer, M. Sutton and G.B. Stephenson, 1991, Mat. Sci. Eng. A **133**, 611.

Kraus, L., K. Zaveta, O. Heczko, P. Duhaj, G. Vlasak and J. Schneider, 1992, J. Magn. Magn. Mater. **112**, 275.

Kubaschewski, O., 1982, Iron – Binary Phase Diagrams (Springer-Verlag, Berlin, Heidelberg, New York).

Kulik, T., T. Horubala and H. Matyja, 1992, Mater. Sci. Eng. A **157**, 107.

Kupfmüller, K., 1990, Einführung in die theoretische Elektrotechnik (Springer-Verlag, Berlin) p. 314.

Kuhrt, C., and L. Schultz, 1993, J. Appl. Phys. **73**, 6588.

Lachowicz, H.K., and A. Slawska-Waniewska, 1994, J. Magn. Magn. Mater. **133**, 238.

Luborsky, F.E., 1961, J. Appl. Phys. **32**, 171S.

Manaf, A., R.A. Buckley and H.A. Davies, 1993, J. Magn. Magn. Mater. **128**, 302.

Müller, M., and N. Mattern, 1994, J. Magn. Magn. Mater. **136**, 79.

Müller, M., N. Mattern and L. Illgen, 1991, Z. Metallk. **82**, 895.

Néel, L., 1954, J. Phys. Radium **15**, 225.

Nielsen, O.V., 1985, IEEE Trans. Magn. **MAG-21**, 2008.

Noh, T.H., M.B. Lee, H.J. Kim and I.K. Kang, 1990, J. Appl. Phys. **67**, 5568.

O'Handley, R.C., J. Megusar, S.-W. Sun, Y. Hara and N.J. Grant, 1985, J. Appl. Phys. **57**, 3563.

Pfeifer, F., 1992, Concise Encyclopedia of Magnetic and Superconducting Materials, ed. J. Evetts (Pergamon Press, Oxford) p. 349.

Pfeifer, F., and C. Radeloff, 1980, J. Magn. Magn. Mater. **19**, 190.

Sawa, T., and Y. Takahashi, 1990, J. Appl. Phys. **67**, 5565.

Schäfer, R., A. Hubert and G. Herzer, 1991, J. Appl. Phys. **69**, 5325.

Sixtus, K., 1962, Z. Angew. Phys. **14**, 241.

Sixtus, K., 1970, Z. Angew. Phys. **28** (1970) 270.

Slawska-Waniewska, A., P. Nowicki, H. K. Lachowicz, P. Gorria, J.M. Barandiarán and A. Hernando, 1994, Phys. Rev. B **50**, 6465.

Suryanarayana, C., 1995, Int. Mater. Rev. **40**, 41.

Suzuki, Y., J. Haimovich and T. Egami, 1987, Phys. Rev. B **35**, 2162.

Suzuki, K., A. Makino, N. Kataoka, A. Inoue and T. Masumoto, 1991, J. Appl. Phys. **70**, 6232; Mater. Trans. JIM **32**, 93.

Suzuki, K., A. Makino, N. Kataoka, A. Inoue and T. Masumoto, 1993, J. Appl. Phys. **74**, 3316.

Suzuki, K., A. Makino, A. Inoue and T. Masumoto, 1994, Sci. Rep. RITU A **39**, 133.

Tonge, D.G., and E.P. Wohlfarth, 1957, Philos. Mag. **2**, 333.

Tonge, D.G., and E.P. Wohlfarth, 1958, Philos. Mag. **3**, 536.

Twarowski, K., M. Kuzminski, A. Slawska-Waniewska, H.K. Lachowicz and G. Herzer, 1995, J. Magn. Magn. Mater. **150**, 85.

Ueda, Y., S. Ikeda and K. Minami, 1994, Mater. Sci. Eng. A **181–182**, 992.

Vacuumschmelze GmbH, 1990, Weichmagnetische Werkstoffe, ed. R. Boll (Siemens AG Verlag, Berlin und München).

Vacuumschmelze GmbH, 1993, Toroidal Cores of VITROPERM, Data sheet PW-014.

Yamamoto, T., 1980, The Development of Sendust and Other Ferromagnetic Alloys (Komiyama Printing, Chiba, Japan) p. 26.

Yelsukov, Ye.P., V.A. Barinov and G.N. Konygin, 1986, Phys. Met. Metall. **62**, 85.

Yoshizawa, Y., and K. Yamauchi, 1989, IEEE Trans. Magn. **MAG**-25, 3324.

Yoshizawa, Y., and K. Yamauchi, 1990a, Mater. Trans. JIM **31**, 307.

Yoshizawa, Y., and K. Yamauchi, 1990b, IEEE Transl. J. Magn. **5**, 1070.

Yoshizawa, Y., and K. Yamauchi, 1991a, Mater. Res. Soc. Symp. Proc. **232**, 183.

Yoshizawa, Y., and K. Yamauchi, 1991b, Mater. Sci. Eng. A **133**, 176.

Yoshizawa, Y., S. Oguma and K. Yamauchi, 1988, J. Appl. Phys. **64**, 6044.